

Article

Scattering of e^{\pm} from CF_3I MoleculeMahmudul H. Khandker ¹, M. Mousumi Khatun ^{1,2}, M. Masum Billah ¹, M. M. Haque ¹, Hiroshi Watabe ³, A. K. Fazlul Haque ^{1,3,*} and M. Alfaz Uddin ¹

¹ Atomic and Molecular Physics Research Laboratory, Department of Physics, University of Rajshahi, Rajshahi 6205, Bangladesh

² Institute of Fuel Research and Development (IFRD), Bangladesh Council of Scientific and Industrial Research (BCSIR), Dhanmondi, Dhaka 1205, Bangladesh

³ Division of Radiation Protection and Safety Control, Cyclotron and Radioisotope Center, Tohoku University, 6-3 Aoba, Aramaki, Aoba, Sendai 980-8578, Japan

* Correspondence: fhaque@ru.ac.bd; Tel.: +880-721-711102

Abstract: Theoretical investigation of the scattering of electrons and positrons from the plasma etching gas trifluoroiodomethane (CF_3I) is presented in the present work. The investigation is carried out by taking into account the screening correction arising from a semiclassical analysis of atomic geometrical overlapping of the scattering cross-sections calculated in the independent atom approximation. The scattering system $e^{\pm}-CF_3I$ is studied through the calculations of the observable quantities, namely, absolute differential, Sherman function, total elastic and inelastic, momentum transfer, viscosity, ionization and total cross sections over the energy range 1 eV–1 MeV. Energy dependency of the differential cross section and Sherman function are also picturized in this work. A comparative study is carried out between scattering observables for electron impact with those for positron impact to get a better understanding of the interaction and dynamics of the collision process. The corresponding scattering quantities of the constituent atoms are calculated employing a complex optical model potential by solving the Dirac relativistic wave equations in the framework of partial wave analysis. The comparison of our results with the available experimental and theoretical data shows a reasonable agreement.

Keywords: electron and positron scattering; molecular scattering; CF_3I ; independent atom model; screening correction



Citation: Khandker, M.H.; Khatun, M.M.; Billah, M.M.; Haque, M.M.; Watabe, H.; Haque, A.K.F.; Uddin, M.A. Scattering of e^{\pm} from CF_3I Molecule. *Atoms* **2022**, *10*, 85. <https://doi.org/10.3390/atoms10030085>

Academic Editor: Grzegorz Piotr Karwasz

Received: 31 July 2022

Accepted: 20 August 2022

Published: 24 August 2022

Publisher's Note: MDPI stays neutral with regard to jurisdictional claims in published maps and institutional affiliations.



Copyright: © 2022 by the authors. Licensee MDPI, Basel, Switzerland. This article is an open access article distributed under the terms and conditions of the Creative Commons Attribution (CC BY) license (<https://creativecommons.org/licenses/by/4.0/>).

1. Introduction

The knowledge of electron–molecule (or atom) collision plays a significant role in understanding the structure of atoms and molecules, the interaction of ionizing radiation with matter, the deposition of energy by radiation in matter, the interactions and transport of electrons in plasmas, and the behavior of electrons in the condensed phases of matter [1]. This fundamental knowledge is of practical importance in many research and technological areas such as magneto-hydrodynamic power generation, material processing applications, manufacturing semiconductor devices, plasma-assisted combustion, modeling of various laser systems, electron beam technology, radiology and dosimetry, mass spectrometry, atmospheric physics, astrophysics, astrochemistry, applied atomic physics, photochemistry, auroras, supernova ejecta, artificial, terrestrial, space and astrophysical plasmas, etc. [2–5]. On the other hand, a comprehensive data set of positron impact molecular scattering cross-sections is required in astrophysical research, radiation-based technologies, and energy deposition models [6]. In addition to general importance, CF_3I carries special attention, as a promising feedstock gas, in the semiconductor plasma industry. Perfluorocarbons, the main feed gases used in the plasma processing industry, are strong greenhouse gases due to their large infrared absorption and long atmospheric lifetime. These environmental reasons have led to an international agreement (under the Kyoto protocol) to phase out the use of

strong greenhouse gases as feedstock gases and find environmentally friendly alternatives of these gases [7]. Hence, it is now a worldwide research need to seek alternative feedstock gases with reduced environmental consequences [7]. To use a new feed gas in the existing plasma industry, a comprehensive set of accurate cross-section data of the scattering of electrons and positrons with the gas is a requisite to run simulations of the reactant plasma.

CF₃I is a promising feedstock gas, in the plasma etching industry, due to its short atmospheric lifetime (<2 days) and its ability of providing copious quantities of reactive species CF⁺ and CF₃ [8]. To use CF₃I as a feed gas, an extended database regarding the scattering of electrons and positrons off the CF₃I is needed. However, both experimental and theoretical databases regarding the scattering system e[±]-CF₃I are sparse. Experimental data is time consuming and expensive. Moreover, there are very few laboratories worldwide that can provide experimental data. Therefore, theoretical investigation is a great option to provide such data. Despite the aforesaid theoretical importance, the theoretical modeling of e[±]-molecule collision is more complex than the corresponding e[±]-atom collision system. Firstly, molecules have more than one center (nucleus), while an atom has one center. The energy spectra of molecules are much more complex than the atomic spectra due to the additional degrees of freedom arising from the motion of the nuclei. Moreover, heteronuclear diatomic molecules and a large number of polyatomic molecules do not have a center of symmetry. This gives rise to a noncentral interaction between the molecular target and the incident lepton [9]. Furthermore, at intermediate and high energies, almost all inelastic channels (excitation, ionization, rotation, vibration, etc.) are open, which makes an ab initio calculation more complex [10]. The advantage is that these complexities do not play a significant role in shaping up cross-sections at intermediate and high energies. Many approximated methods have been proposed to deal e[±]-molecule collision at intermediate and high energies.

The independent atom model (IAM) is one of the fruitful models in which molecular scattering amplitudes are obtained by adding atomic scattering amplitudes multiplied by a phase vector. Thus, in the IAM, interference of scattering waves originating from the different atoms and the geometry of the molecule are taken into account. This model is based on the following assumptions: (i) each atom of the molecule scatters independently; (ii) redistribution of atomic electrons due to molecular binding is unimportant; and (iii) multiple scattering within the molecule is negligible [9]. These assumptions are valid only when de Broglie wavelengths of the incident electron are small in comparison to the inter-atomic distances. Hence, IAM is a high-energy approximation that assumes that the target molecule can be approximately substituted by the constituent atoms in the corresponding positions. Moreover, this model can be applied to arbitrary molecular species as it does not use molecular symmetry consideration [11]. Hence, this approximation opens the possibility of obtaining data for a large number of arbitrary molecular species from a smaller number of atoms. Thus, this model reduces the complex anisotropic e[±]-molecule to the e[±]-atom problem, which is easier to handle.

The incident electrons possess high resolving power when they have de Broglie wavelength $\lambda = 2\pi/k < 2.3$ a. u. and the target molecule becomes fully transparent to them [10,11]. As a result, the consideration of each constituent atom as an independent scatterer works well. However, as the energy falls below 100 eV, the resolving power of the incident electron becomes low and the target does not remain fully transparent. Moreover, since the low energy atomic cross-sections are usually very large (of the order of molecular bond lengths), overlapping of atomic cross-sections would occur inside the molecule if geometrically visualized. Ignoring this overlapping will count each electron interaction with a pair of overlapped atoms twice, and will not account for angular distributions due to multiple dispersions [11]. As a result, IAM overestimates molecular cross-sections at low energy (<100 eV). To extend the validity of IAM to low energies, Blanco et al. [12] proposed a screening correction, arising from a semiclassical analysis of atomic geometrical overlapping, for the scattering cross-section calculations in the IAM. Blanco et al. [12] applied this screening correction to various observables calculated in IAM. Earlier we

applied this screening correction to the scattering observables calculated in the IAM based on Dirac relativistic partial wave analysis [13–15] and significant improvement, as expected, was observed at low incident energies.

In an objective of catering to the raw data need in the aforesaid applications and better understanding the lepton–molecule interaction, screening corrected independent atom model (SCIAM) with complex free-atom optical model potential (OPM) in the fold of Dirac relativistic partial wave analysis has been employed in this work to investigate the e^{\pm} -CF₃I scattering system throughout the calculations of different observable quantities over the energy range 1 eV–1 MeV. The main reason for adopting the Dirac partial wave analysis in this study is that this relativistic approach automatically includes the spin-orbit term, while the Schrödinger equation requires the inclusion of a spin-orbit interaction term separately in the collision dynamics [5,16]. Optical model potential, a complex local potential, consists of two parts—real and imaginary parts. The real part comprises static, exchange, and correlation–polarization potentials. Static potential is determined, in the context of the static-field approximation, from the interaction of incident lepton with the undeformed distribution of nuclear protons and orbital electrons of the target. An approximate local-exchange interaction [17] is added to the electrostatic potential to handle the exchange effects. The deformation of the target charge distribution by the approach of an incident lepton is described by the correlation–polarization potential (CPP), a combination of asymptotic polarization potential [18] and a short range correlation potential [19,20]. The accuracy of real potential is limited by the existence of open inelastic channels above the excitation threshold. A depletion of the elastically scattered electrons or positrons occurs due to the loss of projectile flux from the elastic channel to the inelastic channels. This loss is described by a semi-relativistic imaginary potential [21].

Despite the importance of both theoretical and practical standpoints, data of the scattering system e^{\pm} -CF₃I are sparse in the literature. Most of the experimental data that are available in the literature are on electron-CF₃I scattering. Underwood-Lemons et al. [22] reported TCS, measured using electron transmission spectroscopy, for the scattering process of CF₃I by low energy electron impact. Christophorou and Olthoff [8] published a data compilation recommending data on absolute differential (DCS), total (TCS), momentum transfer (MTCS), total ionization (TICS), total photoabsorption, and total electron attachment cross-sections for e^{-} -CF₃I scattering. Rozum et al. [23] provided a summary on the available experimental and theoretical data suggesting cross-sections for electron scattering (total, excitation, momentum transfer, and elastic integral), electron impact dissociation, and dissociative electron attachment. Kitajima et al. [24] reported experimental DCS in the angular region 20°–130° over the energy range 1.5 eV–60 eV obtained using the relative flow technique. Francis-Staite et al. [25] published experimental DCS (in the angular range of 20°–135°) and integrated elastic cross-sections (IECS) in the energy range 10–50 eV obtained using a cross-beam apparatus. H Cho et al. [26] presented experimental DCS for scattering angles from 10° to 180°, IECS and MTCS, measured with a crossed electron–molecular beam spectrometer, over the incident energy range 5–50 eV. Kiataki et al. [27] calculated DCS and IECS, using Born-corrected static-exchange plus polarization (SEP) approximation, in the low energy region (1.5–12 eV). Nishimura and Nakamura [28] measured TCS for electron scattering, in the energy range 1–3000 eV, using a linear-type electron transmission apparatus. Kawada et al. [29] published experimental TCS, both for electron and positron impact, over the energy range 1–600 eV obtained using the linear transmission method. This is the only available data, to the best of our knowledge, for e^{+} -CF₃I scattering. Theoretical investigation of e^{\pm} -CF₃I collision dynamics is rare. Bettega et al. [30] reported IECS, DCS, and MTCS over the energy range 5–30 eV calculated using the Schwinger multichannel method with the pseudopotentials (SMCPP) method and static-exchange approximation. Antony et al. [7] presented TCS and TICS over the incident energy range 50–2000 eV using the spherical complex potential formalism (SCPF).

Hence, it is clear that the available data is not enough to fulfill the demand. In some works, limited incident energy range is used and, in some works, limited spectrum of observable quantities are reported. The purpose of this theoretical investigation is to present a wide spectrum of scattering quantities namely, DCS, IECS, MTCS, viscosity cross section (VICS), inelastic cross section (INCS), TCS, TICS, and Sherman function of the scattering system $e^\pm\text{-CF}_3\text{I}$ over a wide energy range 1 eV–1 MeV to meet the demand of a detailed database of e^\pm interactions with trifluoroiodomethane in the semiconductor plasma industry and other research and technical areas.

This paper is presented as follows. The mathematical details of this investigation are discussed in Section 2. The results of our proposed model and comparison of our results with the available data are vignettted in Section 3. In Section 4, we have drawn conclusion on our results. In this manuscript, equations are expressed in CGS Gaussian units unless otherwise specified. However, most of the calculations in the FORTRAN code [21] are performed in Hartree atomic units, in which $\hbar = m_e = e = 1$.

2. Outline of the Theory

2.1. The Interaction Potential

The complex free-atom optical potential for the electron and positron scattering has the following form [31]:

$$V(r) = V_{st}(r) + V_{ex}(r) + V_{cp}(r) - iW_{abs}(r). \tag{1}$$

Here, $V_{st}(r)$, $V_{ex}(r)$, and $V_{cp}(r)$, the components of the real part of OPM, represent the static, exchange, and correlation–polarization potential respectively and the imaginary part, W_{abs} represents the absorption potential. For positron, V_{ex} in $V(r)$ is omitted as exchange does not arise due to distinguishability of the projectile positron and bound electrons.

Within the static-field approximation, elastic collision of projectiles, electrons, or positrons, with the target is assumed to reduce to the instantaneous Coulomb interaction. The potential of this interaction, termed as static potential, at a distance r from the nucleus of the target can be written as:

$$V_{st}(r) = ze[\phi(r)], \tag{2}$$

where ze is the charge of the projectile and $\phi(r) = \phi_n(r) + \phi_e(r)$ is the electrostatic potential with $\phi_n(r)$ and $\phi_e(r)$ being the contributions of the nuclear protons and atomic electrons to this potential. Under the static-field approximation, $\phi_n(r)$ and $\phi_e(r)$ can be completely modeled by the spatial charge distributions of nuclear protons, q_n , and that of bound electrons, q_e [21], respectively. Using these density distributions, static potential can now be presented as [32]:

$$\phi(r) = e \left[\int d\mathbf{r}' \frac{q_n(r')}{|\mathbf{r} - \mathbf{r}'|} - \int d\mathbf{r}' \frac{q_e(r')}{|\mathbf{r} - \mathbf{r}'|} \right]. \tag{3}$$

Space densities, q_n and q_e are normalized according to $\int q(r)4\pi r^2 dr = Z$ with Z being the atomic number of the target. Two-parameter Fermi nuclear density [33] and Dirac–Fock electron density, generated within the framework of the multi-configuration relativistic Dirac–Fock method using Desclaux code [34], are used in the present work.

Rearrangement collisions and ejection of bound electrons instead of incoming electrons, arise from the antisymmetrization of the wavefunction of the whole projectile-target system with respect to electrons. This interaction, non-local by nature, is considerably complicated because it involves the solutions of integro-differential equations. It is thus desirable to have an approximation to this non-local potential. A semi-classical local exchange potential of Furness and McCarthy [17] of the following form is used in our present work:

$$V_{ex}(r) = \frac{1}{2}[E - V_{st}(r)] - \frac{1}{2}\{[E - V_{st}(r)]^2 + 4\pi a_0 e^4 q_e(r)\}^{1/2}. \tag{4}$$

Here, E is the impact energy of the electron and a_0 is the Bohr radius.

As the projectile approaches the target, its electric field causes distortion in the atomic electron cloud system. This distortion depends on the separation between the projectile and target. When the projectile is far from the constituent atom, the electric field produced by it over the dimension of target is practically uniform. This electric field induces polarization in the target that acts back on the impinging particle. This asymptotic polarization potential can be approximated as [18]:

$$V_p(r) = -\frac{\alpha}{2(r^2 + d^2)^2} \tag{5}$$

where α is the static polarizability of constituent atom. The constant d can be determined from the following condition:

$$V_p(0) = -\frac{\alpha}{2d^4} = V_{co}(0). \tag{6}$$

Thus

$$d = (-\alpha/2V_{co}(0))^{1/4}. \tag{7}$$

This polarization potential is the same for both electron and positron-atom scattering. However, when the projectile approaches the target sufficiently close, the electric field it produces over the dimension of the target is no longer uniform and the distortion of the electron cloud becomes different for different projectiles. When the projectile penetrates the target, the atomic configuration must adjust for the close proximity of this additional electron or positron. The asymptotic expansion completely breaks down and hence interaction potential for the correlation between the projectile and electron cloud is needed to describe this near-target region interaction. Based on the localized electron in an electron gas, the following correlation potential was given by Perdew and Zunger [19].

$$V_{co}^{(-)}(r) = -\frac{e^2}{a_0} (0.0311 \ln(r_s) - 0.0584 + 0.00133r_s \ln(r_s) - 0.0084r_s), \quad \text{for } r_s < 1 \tag{8}$$

and:

$$V_{co}^{(-)}(r) = -\frac{e^2}{a_0} \beta_0 \frac{1 + (7/6)\beta_1 r_s^{1/2} + (4/3)\beta_2 r_s}{(1 + \beta_1 r_s^{1/2} + \beta_2 r_s)^2} \quad \text{for } r_s \geq 1. \tag{9}$$

where $\beta_0 = 0.1423$, $\beta_1 = 1.0529$ and $\beta_2 = 0.3334$.

For positrons, the correlation potential as given by Jain [20] is:

$$V_{co}^{(+)}(r) = \frac{e^2}{2a_0} \{-1.82r_s^{-1/2} + [0.051 \ln(r_s) - 0.115] \ln(r_s) + 1.167\}, \tag{10}$$

for $r_s < 0.302$,

$$V_{co}^{(+)}(r) = \frac{e^2}{2a_0} [-0.92305 - 0.09098r_s^{-2}] \quad \text{for } 0.302 \leq r_s < 0.56, \tag{11}$$

and:

$$V_{co}^{(+)}(r) = \frac{e^2}{2a_0} \left[-\frac{8.7674}{(r_s+2.5)^3} + \frac{-13.151+0.9552r_s}{(r_s+2.5)^2} + \frac{2.8655}{(r_s+2.5)} - 0.6298 \right] \tag{12}$$

for $0.56 \leq r_s < 8.0$.

For the asymptotic region, $8.0 \leq r_s \leq \infty$, the polarization potential is accurately given by the polarization potential in Equation (5). The parameter r_s is given by the following equation:

$$r_s \equiv \frac{1}{a_0} \left[\frac{3}{4\pi q_e(r)} \right]^{1/3}. \tag{13}$$

The global correlation-polarization potential is determined by combining the long-range Buckingham potential with the short-range LDA correlation potential as follows [31],

$$V_{cp}^{\pm}(r) \equiv \begin{cases} \max\{V_{co}^{\pm}(r), V_{cp,B}(r)\} & \text{if } r < r_{cp} \\ V_{cp,B}(r) & \text{if } r \geq r_{cp}, \end{cases} \quad (14)$$

where r_{cp} is the outer radius at which $V_{co}^{\pm}(r)$ and $V_{pol}(r)$ cross first.

Projectiles with incident kinetic energy greater than the first inelastic threshold are absorbed due to the open inelastic channels above this threshold. The following semi-relativistic absorption potential, W_{abs} is included with the real potential to describe this effect [21]:

$$W_{abs}(r) \equiv \sqrt{\frac{2(E_L + m_e c^2)^2}{m_e c^2 (E_L + 2m_e c^2)}} \times A_{abs} \frac{\hbar}{2} [v_L \rho_e(r) \sigma_{bc}(E_L, \rho_e, \Delta)]. \quad (15)$$

Here, m_e is the mass of the electron and $v_L \sqrt{2E_L/m_e}$ is the non-relativistic velocity corresponding to the local kinetic energy:

$$E_L(r) = \begin{cases} E - V_{st}(r) - V_{ex}(r) & \text{for electron} \\ \max\{E - V_{st}(r), 0\} & \text{for positron.} \end{cases} \quad (16)$$

$\sigma_{bc}(E_L, \rho_e, \Delta)$ is the one-electron cross-section for binary collisions of electrons and positrons of kinetic energy E with a degenerate free-electron gas of density ρ_e , involving energy losses larger than the energy gap Δ and is given by [31]:

$$\sigma_{bc}(E_L, \rho_e, \Delta) = \int_{\Delta/E_F}^{x_{max}} \frac{d\sigma_{bc}}{dx} dx. \quad (17)$$

Here, the Fermi energy, $E_F = \frac{\hbar^2}{2m_e} (3\pi^2 \rho_e)^{2/3}$, $x = W/E_F$ with W being the energy transfer, and:

$$\frac{d\sigma_{bc}}{dx} = \begin{cases} \frac{\pi e^4}{EE_F} \frac{1}{x^2} & \text{for positron} \\ \frac{\pi e^4}{EE_F} \frac{1}{x^2} \left[1 - \frac{x}{E/E_F - x} + \frac{x^2}{(E/E_F - x)^2} \right] & \text{for electron.} \end{cases} \quad (18)$$

For electron scattering, inelastic channels become open above the first excitation energy ϵ_1 . Hence, for the collision of electrons with CF_3I , $\Delta = 4.7$ eV [23]. Since positronium formation is often the first inelastic channel to open for positron scattering and the ionization potentials of CF_3I is greater than the positronium binding energy 6.8 eV, $\Delta = I - 6.8$ eV for positron scattering. For a positron, the maximum allowed energy transfer is the incident kinetic energy of the projectile, i.e., $x_{max} = E/E_F$. Considering Pauli's exclusion principle and exchange interaction it can be shown that $x_{max} = (E/E_F - 1)/2$ for an electron. A_{abs} is an adjustable parameter and its value depends on the projectile-target combination. In the present calculations, the value of the empirical parameter A_{abs} is taken as 2 for an electron and 1.5 for a positron.

2.2. Partial Wave Analysis

The Dirac relativistic equation for a projectile moving with a velocity v in a central field $V(r)$ is given as:

$$[\mathbf{c}\boldsymbol{\alpha} \cdot \mathbf{p} + \beta m_0 c^2 + V_{mC}(r)] \psi(\mathbf{r}) = (E + m_0 c^2) \psi(\mathbf{r}), \quad (19)$$

with $E + m_0 c^2$ being the total energy of the projectile and the operators $\boldsymbol{\alpha}$ and β , the usual 4×4 Dirac matrices. Solutions of the Dirac equation are the spherical waves and are given by:

$$\psi_{E\kappa m}(\mathbf{r}) = \frac{1}{r} \begin{pmatrix} P_{E\kappa}(r) \Omega_{\kappa, m}(\hat{\mathbf{r}}) \\ i Q_{E\kappa}(r) \Omega_{-\kappa, m}(\hat{\mathbf{r}}) \end{pmatrix}, \quad (20)$$

where $P_{E\kappa}(r)$ and $Q_{E\kappa}(r)$ are the upper- and lower-component radial functions and $\Omega_{\kappa,m}(\hat{\mathbf{r}})$ are the spherical spinors. $\kappa = (\ell - j)(2j + 1)$ is the relativistic quantum number with j and ℓ being the total and orbital angular momentum quantum numbers. The radial functions $P_{E\kappa}(r)$ and $Q_{E\kappa}(r)$ of Dirac spherical waves are the solutions of the coupled system of differential equations [35]:

$$\frac{dP_{E\kappa}}{dr} = -\frac{\kappa}{r}P_{E\kappa}(r) + \frac{E - V + 2m_0c^2}{c}Q_{E\kappa}(r) \tag{21}$$

and:

$$\frac{dQ_{E\kappa}}{dr} = -\frac{E - V}{c}P_{E\kappa}(r) + \frac{\kappa}{r}Q_{E\kappa}(r). \tag{22}$$

The spherical waves in Equation (20) are normalized so that the large-component radial function $P_{E\kappa}(r)$ oscillates asymptotically with unit amplitude and takes the following form:

$$P_{E\kappa}(r) \sim \sin\left(kr - \ell\frac{\pi}{2} + \delta_\kappa\right). \tag{23}$$

Here, $k = \frac{p}{\hbar} = \frac{\sqrt{E(E+2m_0c^2)}}{\hbar c}$ is the relativistic wave number of the projectile and $\eta = \frac{qe^2m_e}{\hbar k}$ is the Sommerfeld parameter. Equations (21) and (22) satisfying the asymptotic condition (23), are solved numerically using the subroutine package RADIAL [36] to obtain the global phase shift δ_κ , describing the large r behavior of the spherical wave solutions, and the direct and spin flip scattering amplitudes for the scattering of e^\pm from a central field $V(r)$ as [37,38]:

$$f(\theta) = \frac{1}{2ik} \sum_{l=0}^{\infty} \{(\ell + 1)[\exp(2i\delta_{\kappa=-\ell-1}) - 1] + \ell[\exp(2i\delta_{\kappa=\ell}) - 1]\} P_\ell(\cos\theta), \tag{24}$$

and,

$$g(\theta) = \frac{1}{2ik} \sum_{l=0}^{\infty} [\exp(2i\delta_{\kappa=\ell}) - \exp(2i\delta_{\kappa=-\ell-1})] \times P_\ell^1(\cos\theta) \tag{25}$$

respectively. When ℓ is sufficiently large, the absolute value of the phase shift decreases monotonically with ℓ . The sums in (24) and (25) are carried out up to a maximum angular momentum ℓ_{max} for the largest energies for which δ_κ becomes smaller than $\sim 10^{-9}$. At this point, the partial wave expression for $f(\theta)$ and $g(\theta)$ converge to the required accuracy (usually more than six decimal places) for all angles [21]. Once the phase-shifts and the scattering amplitudes for the constituent atoms are determined, the corresponding projectile-molecule direct and spin flip scattering amplitudes for a given target orientation are given by [38]:

$$F(\theta) = \sum_i \exp(i\mathbf{q}\cdot\mathbf{r}_i) f_i(\theta) \quad \text{and} \quad G(\theta) = \sum_i \exp(i\mathbf{q}\cdot\mathbf{r}_i) g_i(\theta) \tag{26}$$

here, $\hbar\mathbf{q}$ is the momentum transfer by the impinging electron during the collision, \mathbf{r}_i are the atomic positions and $f_i(\theta)$ and $g_i(\theta)$ are the scattering amplitudes for the constituent free atoms of the target. Since the molecule rotates, the corresponding differential cross-section is obtained by averaging over all the orientations of the molecular axis:

$$\frac{d\sigma}{d\Omega} = \langle |F(\theta)|^2 + |G(\theta)|^2 \rangle \tag{27}$$

$$= \sum_{i,j} \frac{\sin(qr_{ij})}{qr_{ij}} [f_i(\theta)f_j^*(\theta) + g_i(\theta)g_j^*(\theta)] \tag{28}$$

$$= \sum_i [|f_i(\theta)|^2 + |g_i(\theta)|^2] + \sum_{i \neq j} \frac{\sin(qr_{ij})}{qr_{ij}} [f_i(\theta)f_j^*(\theta) + g_i(\theta)g_j^*(\theta)] \tag{29}$$

where $q = 2k \sin(\theta/2)$, r_{ij} is the distance between the i -th and j -th atoms, $\sin(qr_{ij})/qr_{ij} = 1$ when $qr_{ij} = 0$ and the term $\sum_{i \neq j}$ represents interference contribution to the molecular differential cross-section.

The integrated elastic σ_{el} , the momentum transfer σ_m , and the viscosity σ_v cross-sections for the projectile-molecule scattering are expressed in terms of the DCS as:

$$\sigma_{el} = \int \frac{d\sigma}{d\Omega} d\Omega = 2\pi \int_0^\pi \left(\frac{d\sigma}{d\Omega} \right) \sin(\theta) d\theta \tag{30}$$

$$\sigma_m = 2\pi \int_0^\pi (1 - \cos \theta) \left(\frac{d\sigma}{d\Omega} \right) \sin(\theta) d\theta \tag{31}$$

$$\sigma_v = 3\pi \int_0^\pi [1 - (\cos \theta)^2] \left(\frac{d\sigma}{d\Omega} \right) \sin(\theta) d\theta \tag{32}$$

The molecular TCS, σ_{tot} , for both electron and positron scattering, sum of integrated elastic (σ_{el}) and absorption cross-section (σ_{inel}), can be obtained as:

$$\sigma_{tot} = \sigma_{el} + \sigma_{inel} = \frac{4\pi}{k} \sum_i \text{Im} f_i(0), \tag{33}$$

with $\text{Im} f_i(0)$ being the imaginary part of the direct scattering amplitude in the forward direction at $\theta = 0^\circ$ for the i -th atom.

To account for the mutual overlapping of nearby atoms in molecules, Blanco and Garcia [11] proposed a screening correction. Accordingly, a semi-classical analysis [11], the screening correction coefficients s_i ($0 \leq s_i \leq 1$), for the i -th atom of a molecule can be given as a sum of $\epsilon_i^{(m)}$ terms, each of them arising from m -atoms overlapping,

$$s_i = 1 - \frac{\epsilon_i^{(2)}}{2!} + \frac{\epsilon_i^{(3)}}{3!} - \frac{\epsilon_i^{(4)}}{4!} + \dots \pm \frac{\epsilon_i^{(N)}}{N!} \tag{34}$$

where:

$$\epsilon_i^{(m)} = \frac{N - m + 1}{N - 1} \sum_{i \neq j} \frac{\sigma_j \epsilon_j^{(m-1)}}{\alpha_{ij}} \quad (m = 2, \dots, N). \tag{35}$$

Here, N is the number of atoms in the target molecule, the j index in sums $\sum_{j(\neq i)}$ runs over all the N atoms except the i one, $\alpha_{ij} = \max(4\pi r_{ij}^2, \sigma_i, \sigma_j)$, σ_i is the atomic cross-sections for the i -th atom of the molecule, and r_{ij} is the distance between centers of atoms i and j . The coefficients s_i refrain from counting each electron interaction with a pair of overlapped atoms twice. Another factor v_{ij} is defined, to quantify the screening corrections to the interference contributions, as $v_{ij} = r_{ij}^2 / (r_{ij}^2 + \rho_{ij}^2)$ with $\rho_{ij} = \max(\sqrt{\sigma_i/\pi}, \sqrt{\sigma_j/\pi}, 1/k)$ being a length dimensional parameter [12]. Since $(\sqrt{\sigma/\pi})$ corresponds to the radius of a circle of area σ , the condition $r_{ij} = \max(\sqrt{\sigma_i/\pi}, \sqrt{\sigma_j/\pi})$ represents a situation of geometrical overlap between two disks for which the center of the smallest one approaches the border of the other. The screening corrected version of Equation (29) can now be written as:

$$\begin{aligned} \left(\frac{d\sigma}{d\Omega} \right)^s = & \sum_i s_i^2 [|f_i(\theta)|^2 + |g_i(\theta)|^2] \\ & + \sum_{i \neq j} v_{ij} s_i s_j \frac{\sin(qr_{ij})}{qr_{ij}} [f_i(\theta) f_j^*(\theta) + g_i(\theta) g_j^*(\theta)] \end{aligned} \tag{36}$$

The first summation in Equation (36) accounts for each atomic contribution, reduced by s_i factor and the second one for the reduced interference contributions. The screening corrected integrated elastic σ_{el}^s , momentum transfer σ_m^s , viscosity σ_v^s cross-sections are obtained from Equations (30)–(32), replacing $\frac{d\sigma}{d\Omega}$ with $(\frac{d\sigma}{d\Omega})^s$ from Equation (36). The screening corrected total σ_{tot}^s cross-section is given by:

$$\sigma_{tot}^s = \sigma_{el}^s + \sigma_{inel}^s = \sum_i s_i(\sigma_{el} + \sigma_{inel}) = \sum_i s_i\sigma_{tot}. \tag{37}$$

The asymmetry function of the randomly oriented molecule is:

$$S(\theta) = i \frac{\langle F(\theta)G^*(\theta) - F^*(\theta)G(\theta) \rangle}{\langle |F(\theta)|^2 + |G(\theta)|^2 \rangle} \tag{38}$$

Since CF₃I is a polar molecule, correction of large-r behavior of the polarization field is required. To do it, it is assumed that the effective dipole polarizability $\alpha_{d,eff}(i)$ of the i -th atom of the molecule is proportional to the polarizability of the free atom, $\alpha_d(i)$, and that the molecular polarizability must be equal to the sum of effective atomic polarizabilities. The effective polarizability used for the calculations of scattering amplitudes from the i -th atom is given by:

$$\alpha_{d,eff}(i) = \alpha_d^{mol} \alpha_d(i) [\sum_j \alpha_d(j)]^{-1} \tag{39}$$

here, the summation extends over all the constituent atoms in molecule.

The total inelastic cross-section σ_{inel} can be partitioned into two main contributions, $\sigma_{inel}(E) = \sum \sigma_{exc}(E) + \sigma_{ion}(E)$, where the first term is the sum over total excitation cross-sections and the second term is the total ionization cross-section. The first term becomes less and less important than the second at energies well above the ionization threshold. Hence, we can write [39]:

$$\sigma_{inel} \geq \sigma_{ion}. \tag{40}$$

In order to determine σ_{ion} from σ_{inel} , an energy dependent ratio $R(E)$ is defined as [39],

$$R(E) = \frac{\sigma_{ion}(E)}{\sigma_{inel}(E)} \tag{41}$$

The ratio $R(E)$ rises steadily as the energy increases above the threshold, and approaches unity at higher energies. To fulfill the requirement that R should be a continuous function of energy for $E \geq I$, the ratio R is presented in the following manner:

$$R(E) = 1 - f(U) = 1 - C_1 \left[\frac{C_2}{U + A} + \frac{\ln U}{U} \right], \tag{42}$$

where $U = E/I$ is the dimensionless variable. The reasons for adopting the above equation are the following. The ratio R increases as E increases above I and approaches unity. The decrease of the function $f(U)$, in the high energy range, must be proportional to $\ln(U)/U$, as the discrete excitation cross-sections, dominated by dipole transitions, falls off as $\ln(U)/U$ at high energies. The term $C_2/(U + A)$ is used to ensure a better energy dependence of $f(U)$ at low and intermediate energies. The adjustable parameters C_1 , C_2 , and A are determined using the following conditions.

$$R(E) = \begin{cases} 0 & \text{for } E \leq I, \\ R_p & \text{for } E = E_p \\ R_F & \text{for } E \geq E_F > E_p. \end{cases} \tag{43}$$

The first condition of Equation (43) implies that no ionization takes place below the ionization threshold energy of the molecule. The ionization potential of CF₃I is taken in this

work as 10.28 eV [40]. Here, E_p is the impact energy at which absorption gets its maximum and R_p represents R at $E = E_p$. In the present analysis, we observe $E_p = 70$ eV for both projectiles. From the discussion of references [39], we choose $R_p = 0.77$. This choice follows from the general observation that at energies close to the peak of ionization, the contribution of the molecular σ_{ion} is about 70–80% in the total inelastic cross-sections σ_{inel} . At incident energies $E \geq E_F$, beyond the peak position E_p , the value of R increases to R_F (very close to 1). To obtain optimal fit with the experimental observations, the value of R_F is chosen as 0.98 at $E_F = 700$ eV. The numerical values of the parameters C_1 , C_2 , and A are, respectively, found to be 0.945, 6.055, 4.719 both for electron and positron scattering. These values are obtained from the solutions of Equation (43) using a FORTRAN program.

3. Results and Discussion

In this work, ELSCATM code [21], based on the solution of Dirac relativistic partial wave equations employing a complex optical potential, is used to calculate the observable quantities of the e^\pm -CF₃I collision system over the energy range 1 eV–1 MeV using single scattering independent atom approximation. Interaction potential of the incident lepton with the constituents of the target molecule is provided by the free-atom complex optical potential (Equation (1)). The phase shifts, δ_κ , required for the calculations of scattering amplitudes are calculated first from the solutions of the Dirac equations up to a matching distance and then for matching with the known exterior solution. Then, using the obtained scattering amplitudes multiplied by a phase vector, various scattering observables for spin-unpolarized electrons or positrons are calculated. Finally, screening corrections of the calculated observables are taken into consideration to extend the low energy validity of this investigation. If partial-wave analysis is feasible, the calculated DCSs, integrated cross-sections, and Sherman function are usually accurate to within about 0.01%. This error estimate refers only to the accuracy of the numerical calculation, and is based on the assumption that the adopted central potential represents the true interaction [21]. Both screened (SCIAM) and unscreened (IAM) calculations are presented in this paper.

In Figure 1, we present our DCS calculations at energies 5, 10, 12, 15, 20, and 25 eV and compare with the available experimental [24–26] and theoretical data [27,30]. In Figure 1a, our calculations show reasonable agreement with the experimental observation of H Cho et al. [26], while the SMCPP calculations of Bettega et al. [30] show excellent agreement and the Born-corrected SEP calculations of Kiataki et al. [27], quite reasonable agreement with the data [26] except at small scattering angles. Two minima are observed in the experimental DCS. The first one is a shallow minimum, observed at $\sim 60^\circ$, and the second one is a deep minimum, observed at $\sim 120^\circ$. Our models, both IAM and SCIAM, can predict the deep one but fails to reproduce the shallow one, while other calculations [27,30] can predict both the minima. At 10 eV, our SCIAM calculations show quite reasonable agreement and SMCPP calculations of Bettega et al. [30], excellent agreement with the observation of H Cho et al. [26] and Kitajima et al. [24]. All the DCS data, experimental and theoretical, available at 10 eV, including ours, disagree significantly with that of Francis-Staite et al. [25] at larger angles ($>90^\circ$). Although two minima are witnessed in the angular distribution of the elastically scattered electrons of 12 eV, one at $\sim 60^\circ$ and another at $\sim 120^\circ$, our models predict one deeper minimum near 105° . In Figure 1d, our SCIAM calculations show reasonable agreement with the experimental data [25,26] and predict a deeper minimum near 105° , while the SMCPP calculations of Bettega et al. [30] show better agreement. Our IAM calculations overestimate DCS at forward angles. In Figure 1e, SCIAM calculations show quite reasonable agreement with the experimental observation [24–26] through the reproduction of the minimum at $\sim 45^\circ$ and the hump at around 70° followed by a minimum at 105° . The depth of the second minimum predicted by our calculations is greater than the observed one. The SMCPP calculations of Bettega et al. [30] predict only one minimum at around 80° . Our IAM calculations overestimate DCS in the forward scattering region. In Figure 1d, our calculations show quite reasonable agreement with the experimental data of Francis-Staite et al. [25].

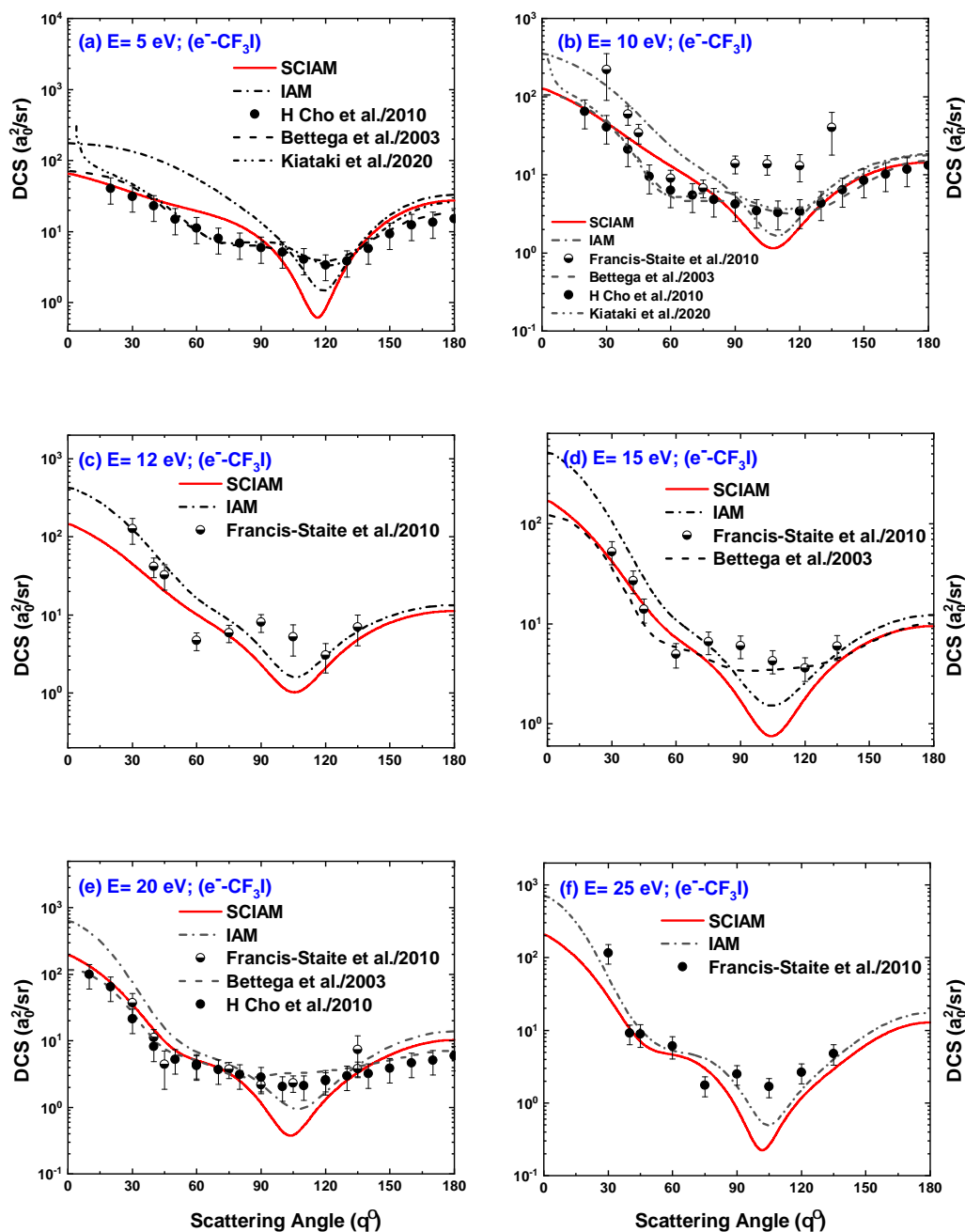


Figure 1. DCS (a_0^2/sr) for the elastic scattering of electrons from CF_3I at incident energies 5, 10, 12, 15, 20 and 25 eV. Theoretical works: SCIAM, IAM, Bettega et al. [30] and Kiataki et al. [27]. Experimental works: Francis-Staite et al. [25], H Cho et al. [26], and Kitajima et al. [24].

In Figure 2, the SMCPP calculations of Bettega et al. [30] show good agreement with the observed DCS [25,26], while our SCIAM method shows quite reasonable agreement. The depth of the minimum, predicted by our model, is greater than the observed one as seen at other low incident energies depicted in Figure 1. Our IAM calculations overestimate data both at small and large angles. In Figure 2b–d, we compare our SCIAM and IAM calculations with the experimental observation of Francis-Staite et al. [25]. Our SCIAM calculations show reasonably good agreement with the observed data, while IAM calculations overestimate the small angle DCS data. In Figure 2e, our SCIAM calculations agree with one or another set of observed data [25,26]. Our calculations show reasonable agreement with the observed data in Figure 2f. It is observed from Figures 1 and 2 that the Born-corrected

SEP calculations of Kiataki et al. [27] and SMCPP calculations of Bettega et al. [30] show better agreement with the low energy DCS data [25,26] than our SCIAM calculations. Our method fails to reproduce the shallow minimum observed at around 60° in the DCSs and predict the depth of the second minimum at 5, 10, 12, and 15 eV. Perhaps these failures of our method arise due to the low energy limitation of optical potential and semi-classical nature of the screening correction. However, the aforementioned models [27,30] are specifically designed for low energy calculations, while our model is designed for the calculations of a broad spectrum of scattering observables over a wide energy range (1 eV–1 MeV). Experimental data for the angular distribution of elastically scattered electrons of energy up to 60 eV is available in the literature. To the best of our knowledge, no high energy DCS data is available. We present our screened and unscreened calculations, depicted in Figure 3, for future reference. Monotonous behavior is observed in DCS above 2500 eV. This is due to the incoherent interference of a large number of angular momentum states.

An important point is observed that, at high energies, both of our calculations, SCIAM and IAM, predict the same. At high incident energies, the de Broglie wavelength of the incident lepton is low. The incident lepton possesses high resolving power due to this smaller value of the de Broglie wave and hence the target molecule becomes fully transparent. Therefore, considering the constituent atoms as independent scatterer causes no significant error. Moreover, high energy atomic cross-sections are not large enough to become overlapped. Therefore, the effect of screening correction diminishes at high incident energies and SCIAM and IAM provide the same results. Furthermore, in low-energy scattering, the projectile gets enough time to scan the features of the target. This scanning of the target is manifested through the structures observed in low-energy DCSs. Due to the high energy approximation, IAM can not picturize this manifestation properly and, hence, IAM and SCIAM differ. On the contrary, at high energies, the projectile just sweeps through without paying attention to the details. As a result, monotonous behavior is observed in high-energy DCS. Hence, the requirement of screening correction becomes negligible in the high-energy region and IAM and SCIAM predict the same.

DCSs of elastically scattered positrons off the plasma etching gas CF_3I are depicted in Figures 4 and 5. To the best of our knowledge, no positron impact DCS data, experimental or theoretical, are available in the literature. We compare our calculations, both SCIAM and IAM, with the data generated by employing the additivity rule on the atomic DCS data of Dapor and Miotello [41] at incident energies 0.5 keV to 4 keV and an excellent agreement is observed. The agreement is not unexpected as the screening corrections play a negligible role at high incident energies due to the small atomic cross-section and high resolving power associated with the high energy positron.

Sherman functions for the $e^\pm\text{-CF}_3\text{I}$ collision system are presented for the first time, to the best of our knowledge, in Figures 6 and 7. An extremum is observed at $\sim 110^\circ$ in the angular distribution of the Sherman function of electrons scattered elastically at 10 eV. It is observed that as the energy of the impinging electron increases, the magnitude of the extremum decreases and its peak shifts toward the left. Comparing Figure 6 with Figures 1 and 2, we see that the angular position of the peak of S matches with the angular position of the minimum of the differential cross-section at the same incident energy. This close relation of the angular position of the extreme value of S and the minimum in DCS is well established in the literature [42]. Therefore, the pattern observed in the calculated angular distribution of the Sherman function of electrons scattered elastically from the CF_3I molecule, manifests the behavior of experimental DCS data. In Figure 7, we illustrate the Sherman function for $e^+\text{-CF}_3\text{I}$. It is observed that the sign of S does not change over the whole angular range or with the increase of energy. This observation reflects the fact that there is no significant minimum in positron impact DCSs of CF_3I .

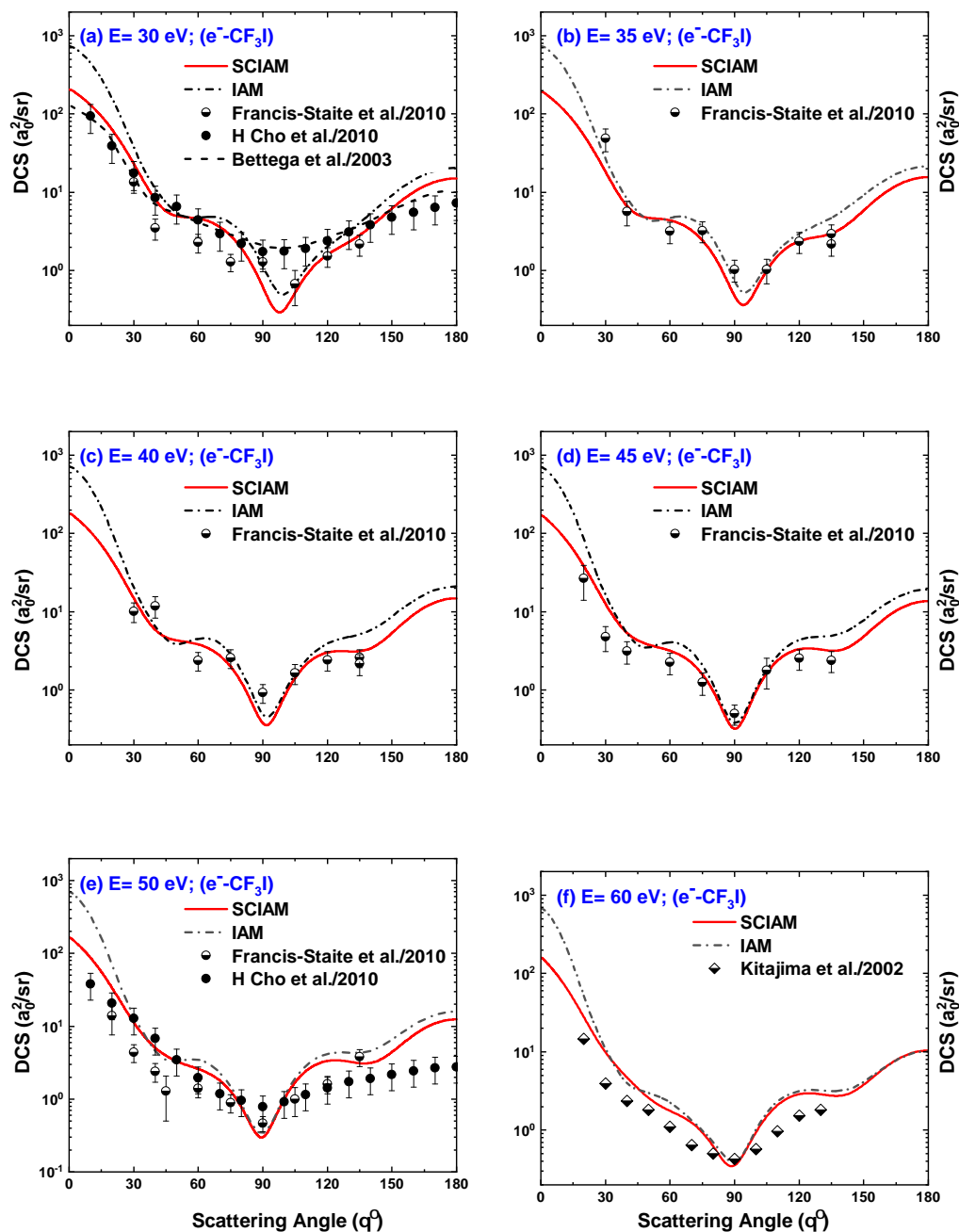


Figure 2. DCS (a_0^2/sr) for the elastic scattering of electrons from CF_3I at incident energies 30, 35, 40, 45, 50, and 60 eV. Theoretical works: SCIAM, IAM, and Bettega et al. [30]. Experimental works: Francis-Staite et al. [25], H Cho et al. [26], and Kitajima et al. [24].

In Figure 8, we present the energy dependence of the angular distribution and Sherman function of the elastically scattered electrons of incident energy 1 eV–1 MeV. It is seen from Figure 8a,c,e that, above ~ 5 eV, our SCIAM calculations agree with one or another set of experimental data. Below ~ 5 eV, our calculations underestimate the experimental DCS at forward angles and overestimate at backward angles. The failure of screened calculations at very low energy is due to the semi-classical nature of the screening correction and the low energy limitation of the optical model. Oscillations are observed below 1 keV in the energy dependent elastic DCS at $\theta = 120^\circ$. The oscillatory pattern is prominent in the energy dependent Sherman function, as seen from Figure 8b,d,f, both at forward and backward scattering angles. This pattern is mainly due to the contribution of the exchange potential [15].

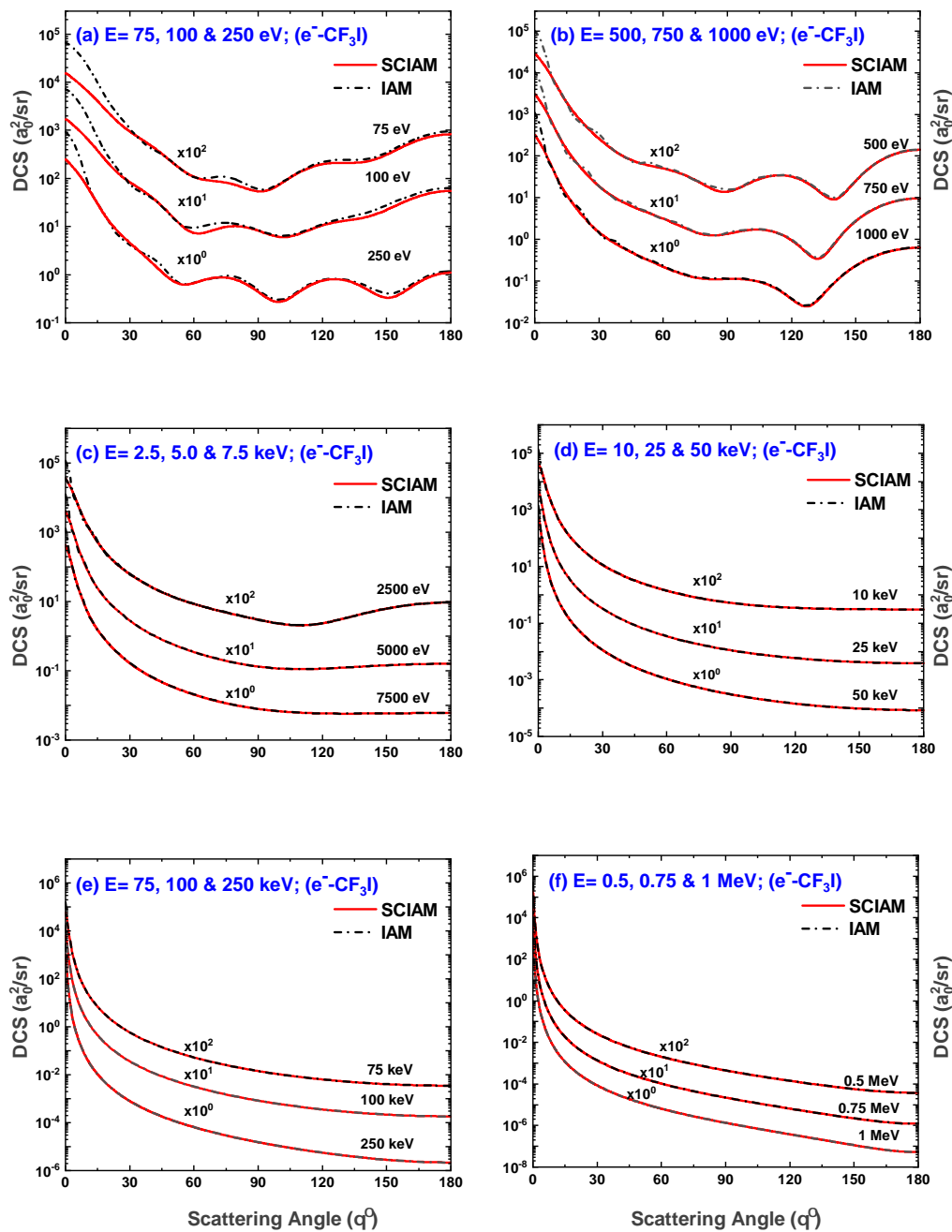


Figure 3. DCS (a_0^2/sr) for the elastic scattering of electrons from CF_3I at incident energies 75, 100, 250, 500, 750, 1000, 2500, 5000, 7500 eV, 10, 25, 50, 75, 100, 250 keV, 0.5, 0.75, and 1 MeV. Theoretical works: SCIAM, IAM.

The energy dependency of the absolute DCS and Sherman function for elastically scattered positrons from CF_3I are presented in Figure 9. Our SCIAM calculations for DCS show excellent agreement with the theoretical data [41] generated by employing the additivity rule. Above 100 eV, a monotonous decrease in DCS is observed. No oscillatory structure is found in the energy-dependent Sherman function, except an extremum above 500 keV. Perhaps this smoothness, both in the DCS and Sherman function, is mostly due to the absence of exchange potential in the case of positron scattering.

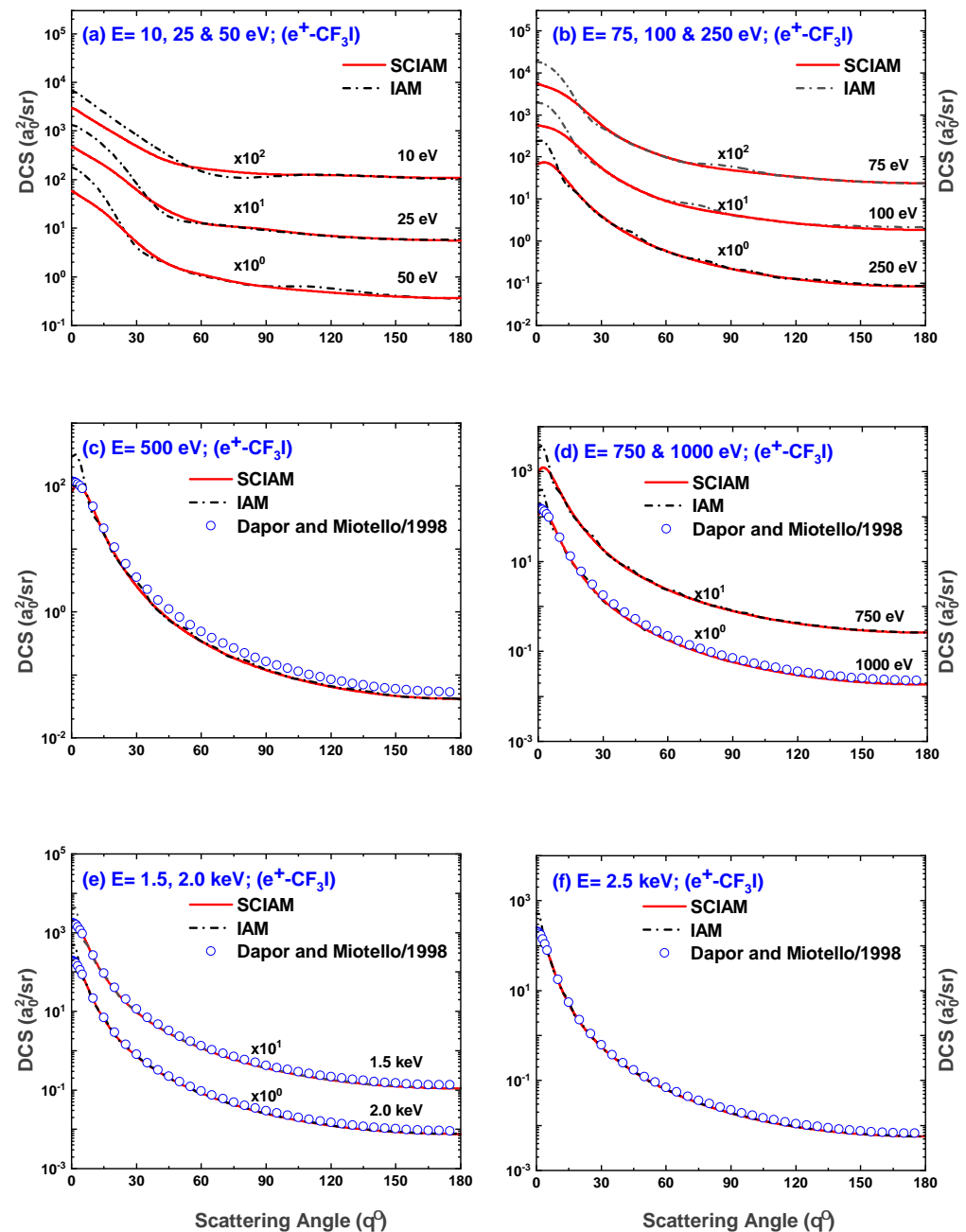


Figure 4. DCS (a_0^2/sr) for the elastic scattering of positrons from CF_3I at incident energies 10, 25, 50, 75, 100, 250, 500, 750, 1000, 1500, 2000, and 2500 eV. Theoretical works: SCIAM, IAM, and Dapor and Miotello [41].

In Figure 10a, we present our SCIAM and IAM calculations of TCS for the scattering of electrons off the trifluoriodomethane molecule and compare with the available experimental data [28,29] and the SCPF calculations of Antony et al. [7]. Our SCIAM model shows excellent reproduction of experimental observations [28,29]. However, our unscreened model overestimates the cross-section data below 100 eV. This low energy overestimation occurs mainly for not considering the large value de Broglie wavelength of the incident lepton and the overlapping of large atomic cross-sections. In SCIAM calculations, this overlapping is taken into consideration to extend the validity of IAM to low energy. Enhancement of TCS is observed in the energy region 5–10 eV. This enhancement is due to the presence of shape resonances [22,27] in the low energy e^-CF_3I collision. These resonances

are the formation of temporary anions caused by the trapping of incoming electrons by the e^- -molecule potential resulting from a combination of short-range attractive and long-range repulsive forces caused by the angular-momentum barrier [43]. The enhancements of TCS are the consequence of the constructive interference of the quasistationary waves reflected back and forth in the inner region of this potential. Underwood-Lemons et al. [22] and Kiataki et al. [27] reported a broad shape resonance at around 5 eV and the other one at around 9 eV. Our model reproduces the first broad shape resonance quite satisfactorily with a peak at around 6 eV but fails to predict the second one. Instead of producing a peak, our model produces a plateau at around 10 eV.

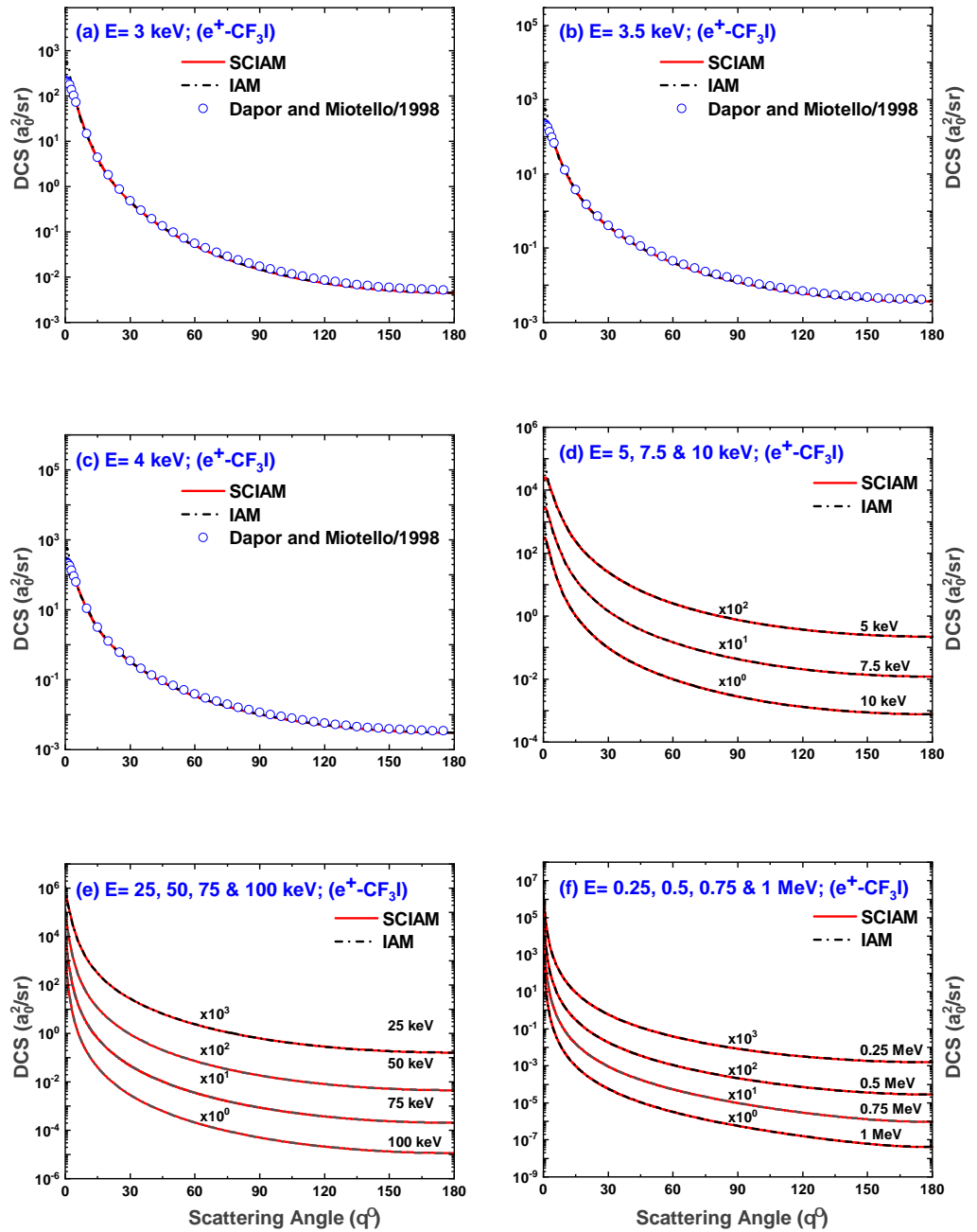


Figure 5. DCS (a_0^2/sr) for the elastic scattering of positrons from CF_3I at incident energies 3, 3.5, 4, 5, 7.5, 10, 25, 50, 75, 100, 250, 500, 750, and 1000 keV. Theoretical works: SCIAM, IAM, and Dapor and Miotello [41].

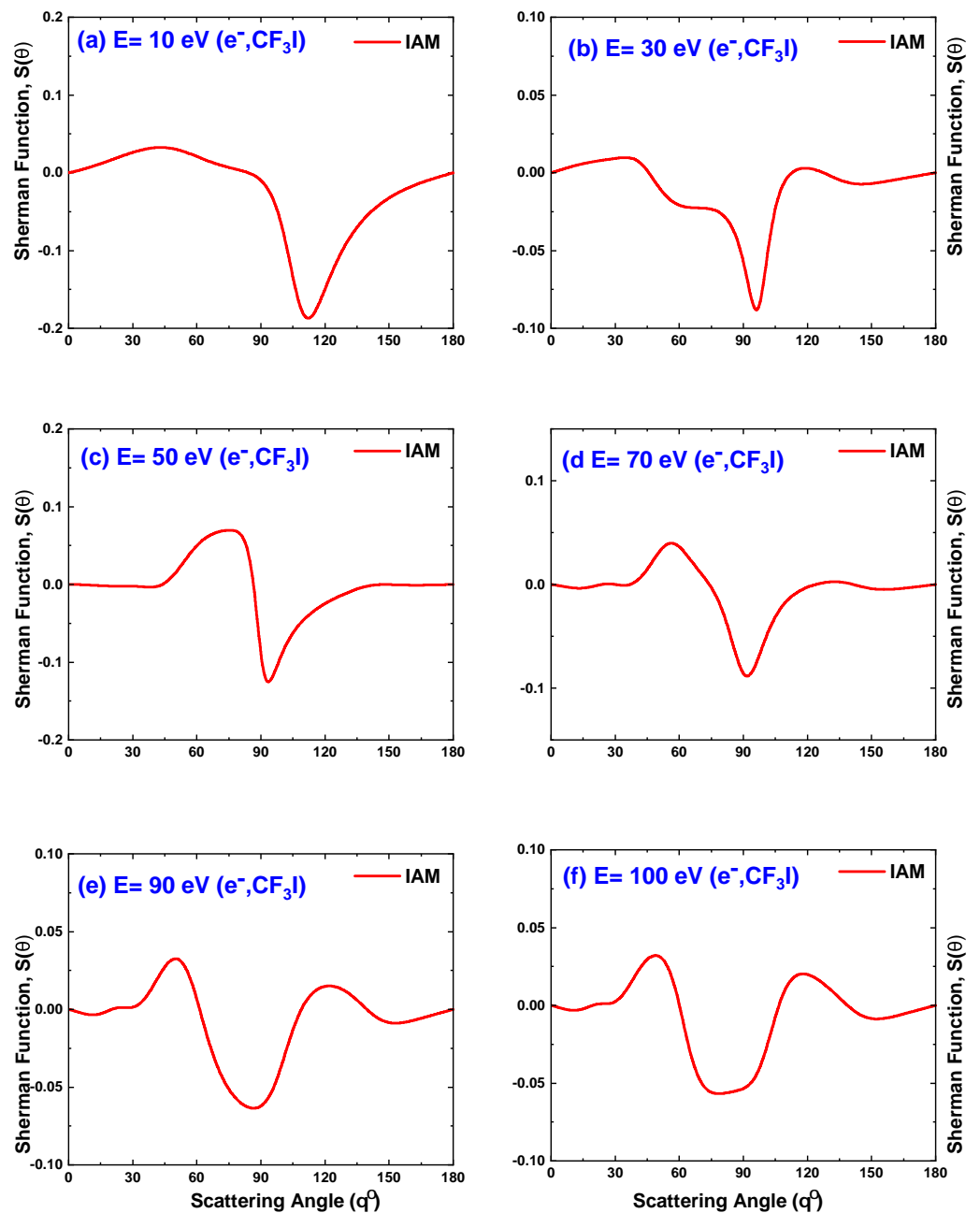


Figure 6. Sherman function for the elastic scattering of electrons from CF_3I at incident energies 10, 30, 50, 70, 90, and 100 eV. Theoretical works: IAM.

From the excellent agreement between our prediction and the experimental observation [28,29], it can be said that the screening correction improves the prediction impressively for a polyatomic molecule such as trifluoroiodomethane. At high energies, both SCIAM and IAM predict the same due to the negligible effect of screening correction. In Figure 10b, we compare our IECS calculations with the available experimental data [24–26] and the theoretical prediction of Mayol and Salvat [44] generated by employing the additivity rule. Our IAM calculations overestimate the data below 100 eV as usually. Improvement of low-energy calculations, taking screening correction into consideration, is eye-catching. We present transport cross-sections, MTCS in Figure 10c, and VICS in Figure 10d, and compare with the available experimental data [24] and theoretical prediction [30,44]. Our SCIAM calculations show excellent agreement with both forms of data. The effect of screening correction is observed to diminish above 100 eV. In Figure 10e, we pictured

INCS. Since there is no data available in the literature, we present it for future reference. TICS for the scattering of electrons from CF_3I is depicted in Figure 10f and compared with the experimental [45] and theoretical data [7]. Our SCIAM calculations show quite good agreement with the experimental data [45]. Our prediction slightly disagrees with that of Antony et al. [7] above ~ 200 eV.

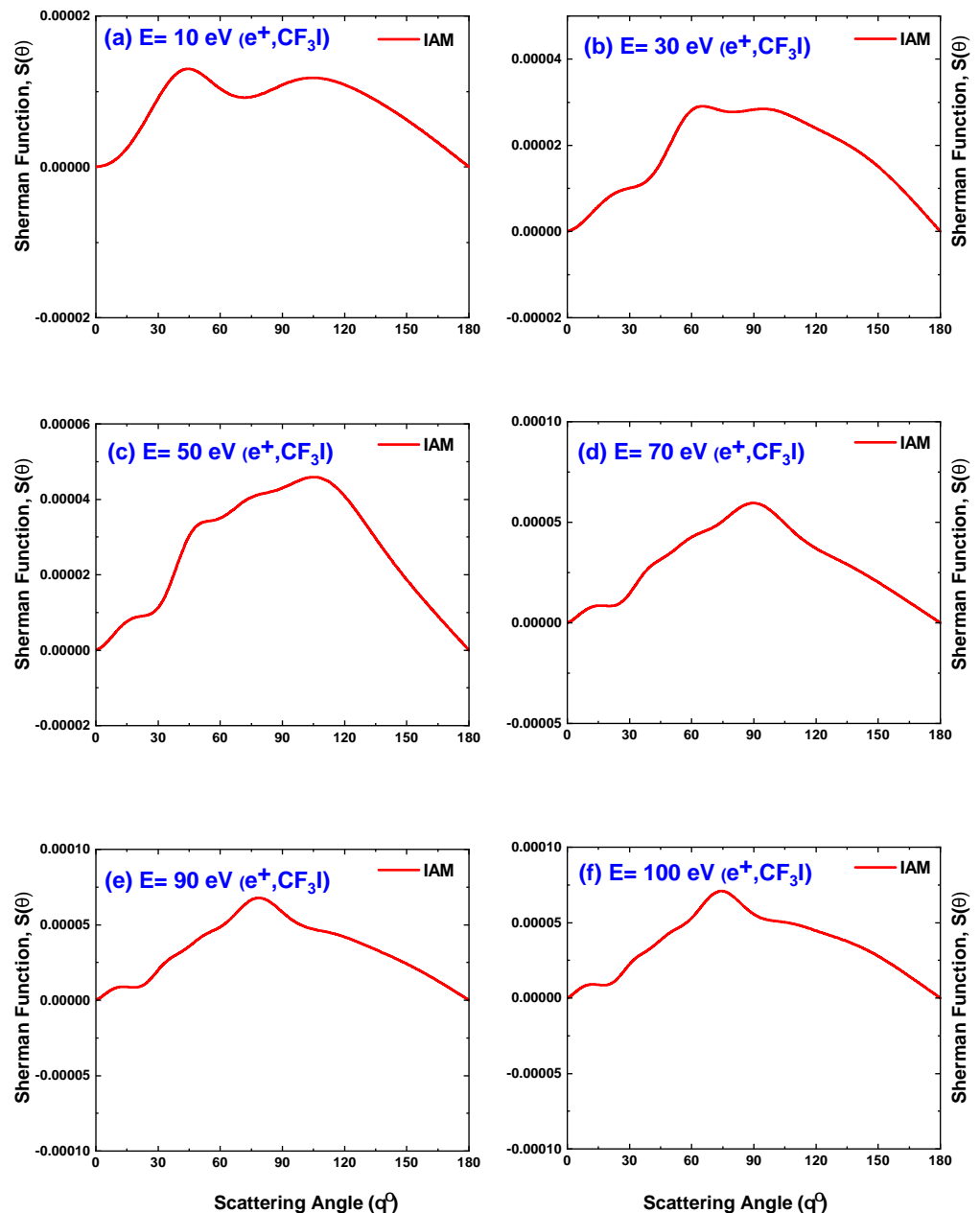


Figure 7. Sherman function for the elastic scattering of positrons from CF_3I at incident energies 10, 30, 50, 70, 90, and 100 eV. Theoretical works: IAM.

We calculate TCS for the scattering of positrons from CF_3I using SCIAM and IAM models and depict the comparison of our prediction with the only available experimental data [29] in Figure 11a. Both model fail to predict the cross-section below 10 eV and a slight over estimation is observed above 10 eV. We present IECS, MTCS, and VICS in Figure 11b–d, respectively, and compare our results with the additivity data [41]. A very good agreement is observed between the data. In Figure 11e,f, we depict our INCS and TICS results. There is no data available in the literature to compare with. Hence, it could be a reference for future researchers.

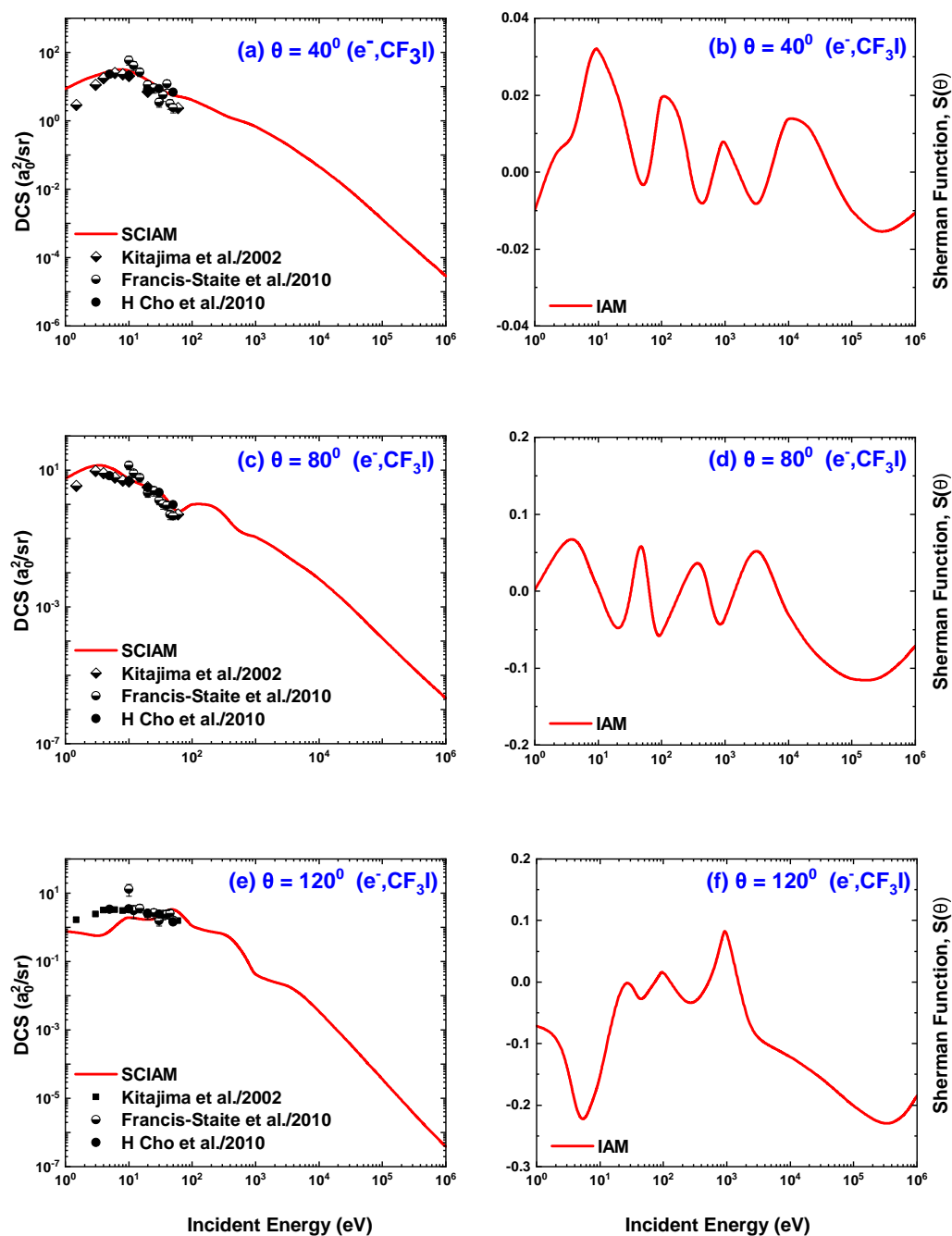


Figure 8. Energy-dependent DCS (a_0^2/sr) and Sherman function at 40° , 80° , and 120° for the elastic scattering of electrons from CF_3I . Theoretical works: SCIAM (DCS), IAM (Sherman function). Experimental works: Francis-Staite et al. [25], H Cho et al. [26], and Kitajima et al. [24].

A comparison between the observable quantities for electron impact with those for positron impact are presented in Figure 12 to exhibit the similarity and dissimilarity arising out of the difference of the interactions of the leptons with the target molecule. It is seen that most of the differences occur in the energy range 1 eV–1 keV. In Figure 12a, we see that DCS for electron impact is larger than that for positron impact. The correlation-polarization and the static interaction have the same sign for electron scattering and a different sign for positron scattering. Hence, the cumulative effect of these two is subtractive for positron impact and additive for electron impact [46]. Due to this subtractive contribution and the absence of exchange potential, the DCS for positron scattering is smaller than that for electron scattering at low energy.

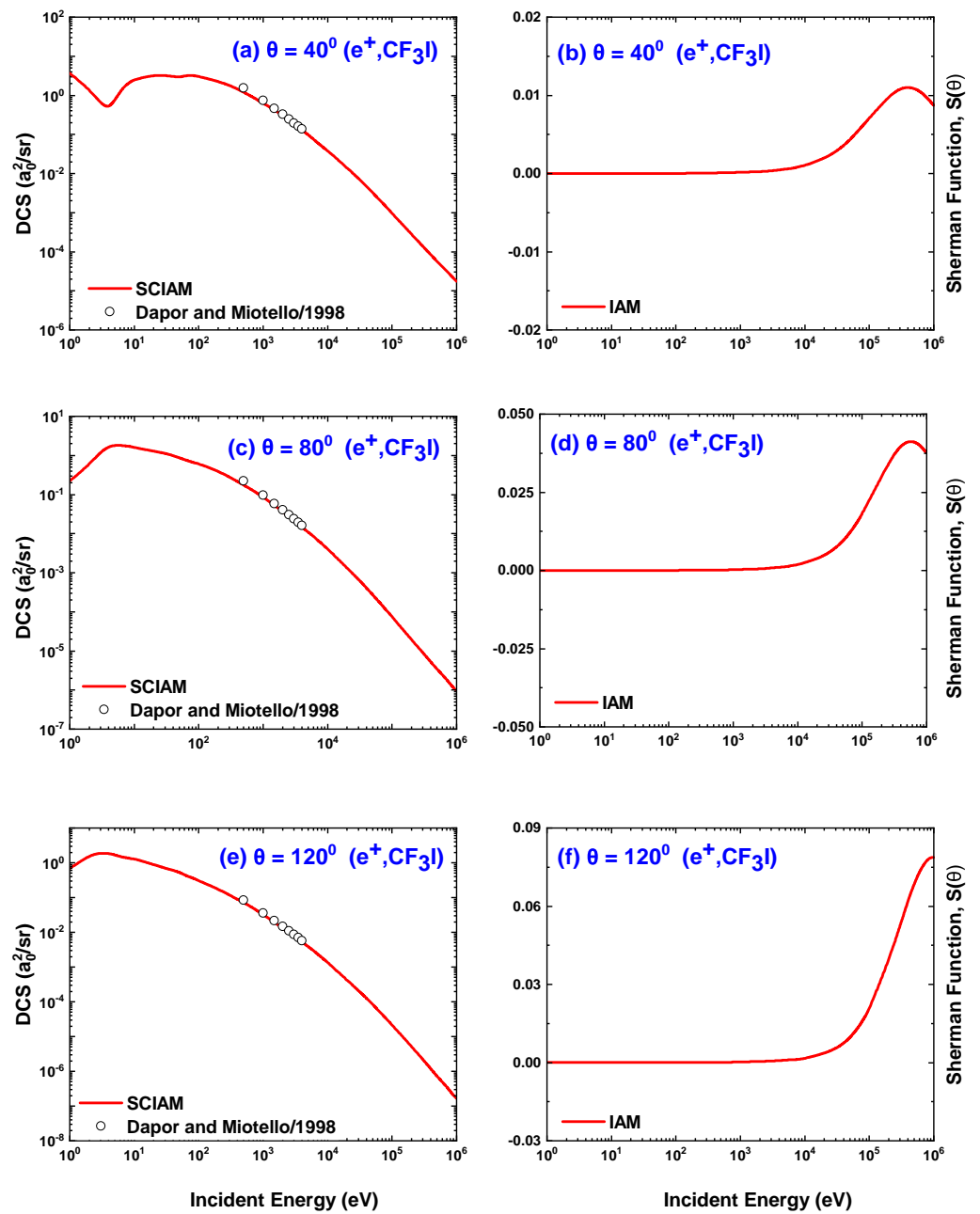


Figure 9. Energy-dependent DCS (a_0^2/sr) and Sherman function at 40° , 80° , and 120° for the elastic scattering of positrons from CF_3I . Theoretical works: SCIAM (DCS), IAM (Sherman function), and Dapor and Miotello [41].

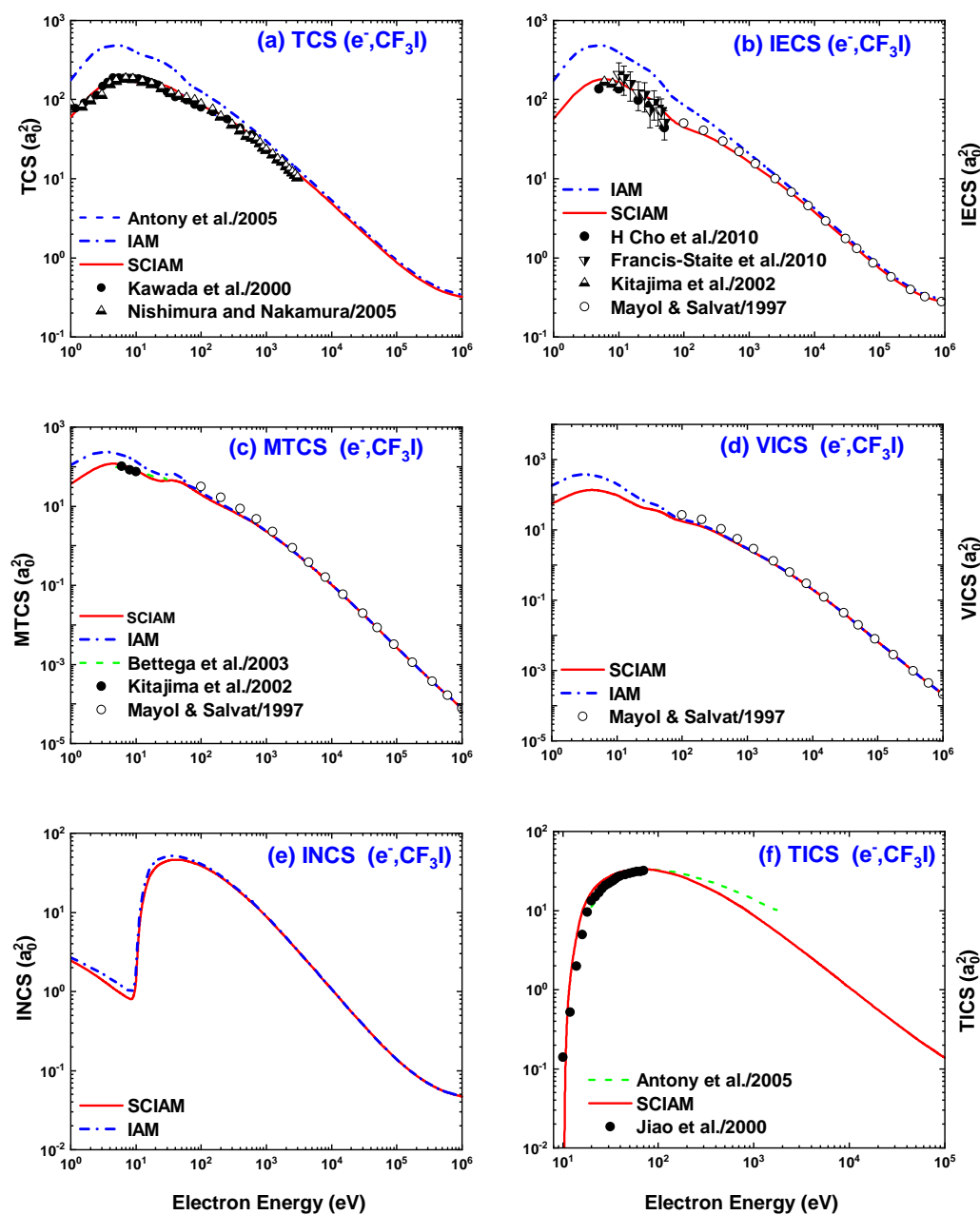


Figure 10. (a) TCS, (b) IECS, (c) MTCS, (d) VICS, (e) INCS, and (f) TICS for the scattering of electrons from CH_3I . Theoretical works: IAM, SCIAM, Antony et al. [7], Bettega et al. [30], and Mayol and Salvat [44]. Experimental works: Kawada et al. [29], Nishimura and Nakimura [28], Francis-Staite et al. [25], Kitajima et al. [24], H Cho et al. [26], and Jiao et al. [45].

At high incident energies, the effect of exchange and polarization potentials diminishes and the static potential starts to dominate. Hence, the difference between the high energy cross-sections for both projectiles also diminishes. Oscillatory behavior is observed in the Sherman function for electron scattering and smooth behavior, for positron scattering. Perhaps, this is due to the exchange potential. In Figure 12c, we present the comparative picture of TCSs for $e^\pm\text{-CF}_3\text{I}$ collision. It is observed that as the energy decreases below 100 eV, TCS for electron impact starts to increase over that for positron impact and below 3 eV these two cross-sections almost merge. This energy region (3–100 eV) is the resonance region, in which temporary capture of the incident electron by the target molecule occurs. The magnitude of TCS for electron impact increase due to the shape resonances and the

effects mentioned in the case of DCS comparison. As the energy increases, the effect of resonance and exchange and polarization potential decreases and so the difference in magnitude of these two TCSs almost vanishes. In Figure 12d, we compare IECSs for e^{\pm} -CF₃I. A large difference in magnitude is observed at low energy, but as the energy increases, this difference mitigates. A similar picture is observed in Figure 12e,f in the case of MTCSs and VICSSs.

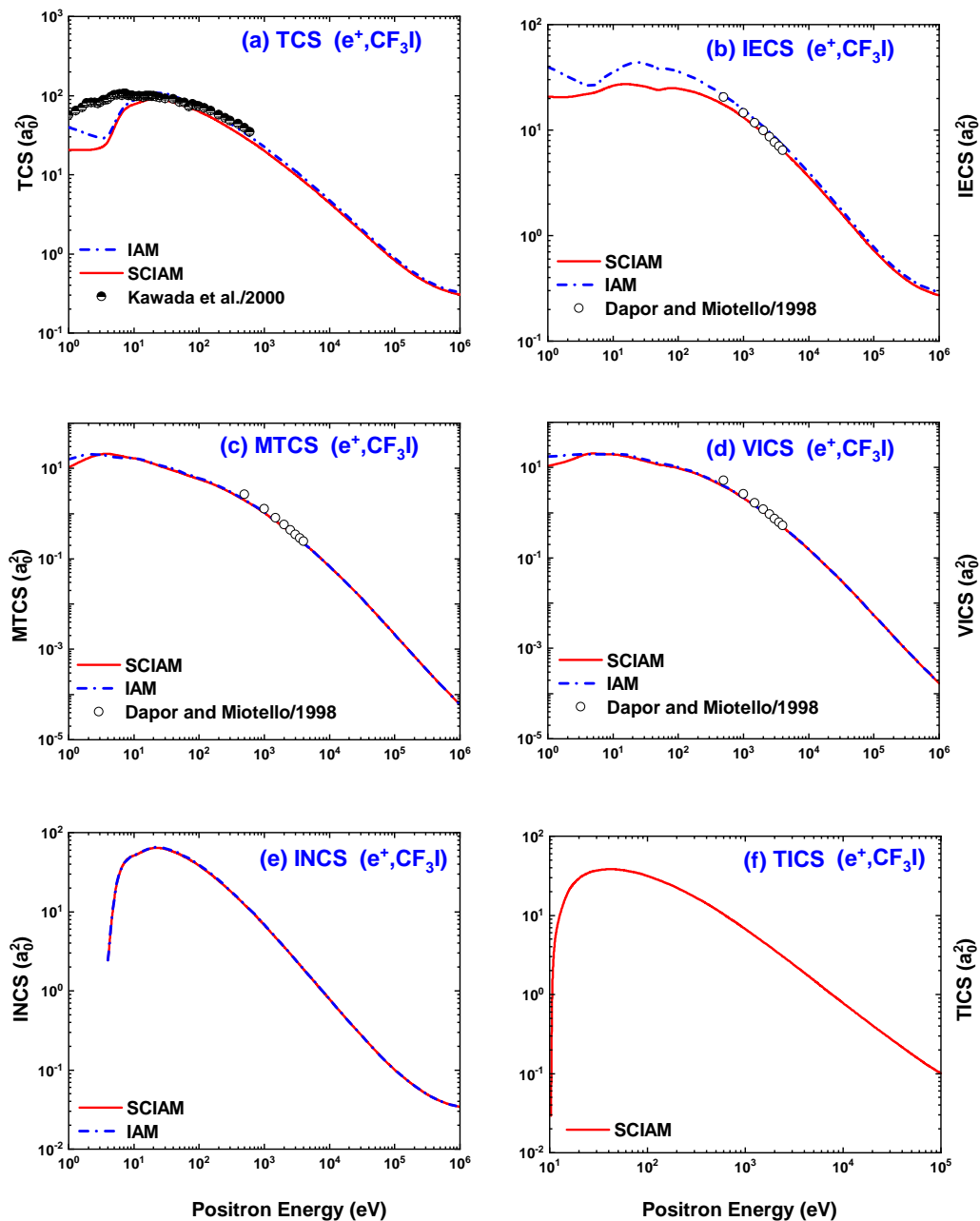


Figure 11. (a) TCS, (b) IECS, (c) MTCS, (d) VCS, (e) INCS, and (f) TICS for the scattering of positrons from CF₃I. Theoretical works: IAM, SCIAM, Dapor and Miotello [41]. Experimental works: Kawada et al. [29].

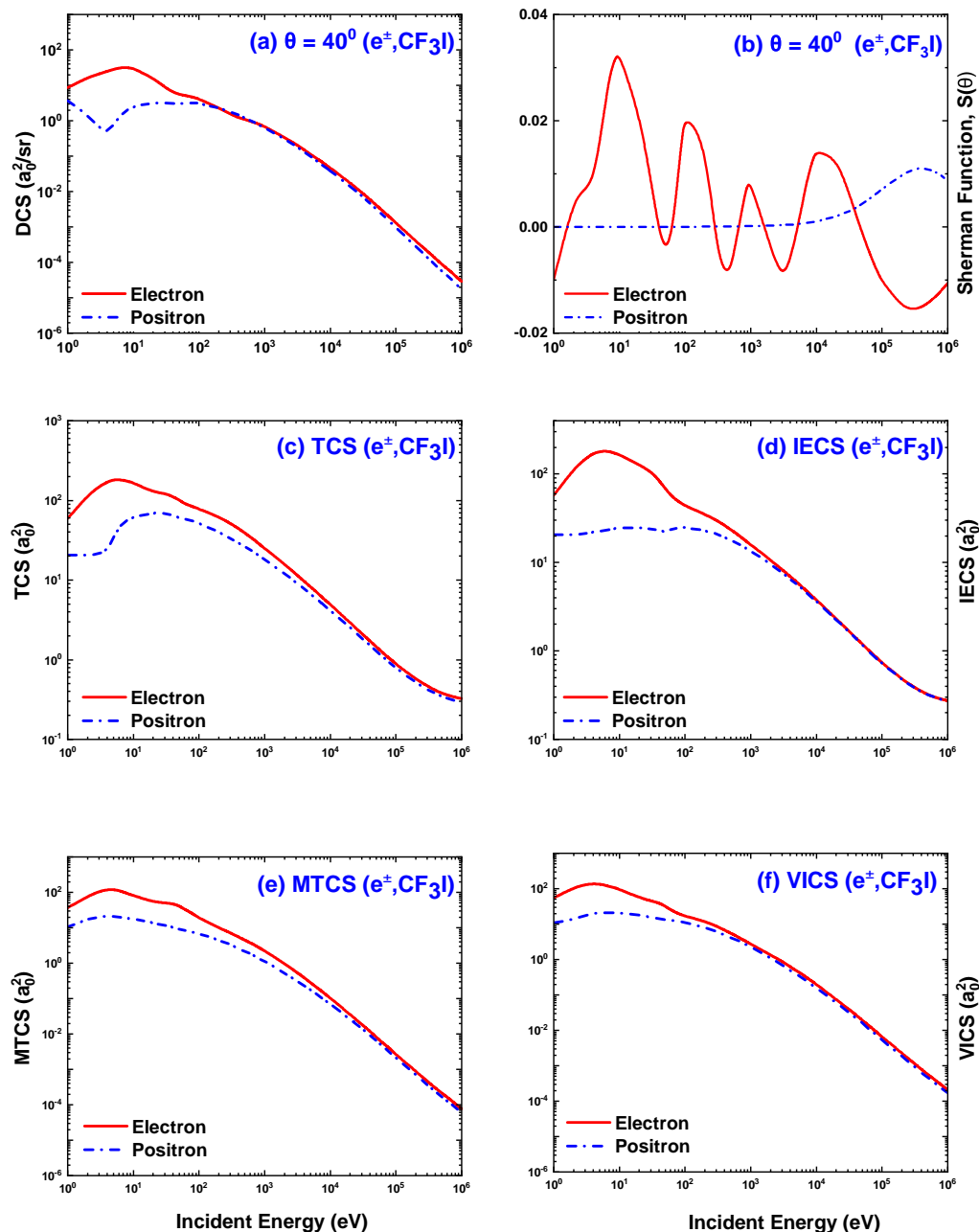


Figure 12. Comparison of the energy dependence of (a) DCS, (b) Sherman function, (c) TCS, (d) IECS, (e) MTCS, and (f) VICS between the e⁻-CF₃I and e⁺-CF₃I scattering. Theoretical works: Electron and Positron.

4. Conclusions

In the present work, we report theoretical investigation throughout the calculations of the observable quantities of the scattering system e[±]-CF₃I over a wide energy range 1 eV–1 MeV using IAM. The scattering amplitudes of the constituent atoms are calculated in the framework of Dirac partial wave analysis employing a free-atom local complex optical potential. The collision dynamics is studied in terms of effective local potential instead of non-local potential to avoid strenuous and prolonged computation. A screening correction, arising from a semiclassical analysis of atomic geometrical overlapping, of the scattering cross-sections calculated in the independent atom approximation is taken into consideration to extend the validity of IAM to the low energy region [12]. We compare our

calculated results with the available experimental and theoretical data and a quite reasonable agreement is observed. From the comparison, it is observed that the incorporation of the screening correction improves the quality of the predicted results both at low energies and angles.

Our DCS calculations, using SCIAM, for electron impact show reasonable agreement below 30 eV and quite good agreement above this energy. Low energy failure of our calculations arises due to the semi-classical nature of the screening correction, low energy limitation of the optical model, and ignoring the multiple scattering. We compare our high energy DCS calculations, using SCIAM and IAM and the additivity rule for both the projectiles and a very good agreement among these three is observed. The result was not unexpected as the screening correction becomes negligible at high incident energies. For the first time, to the best of our knowledge, calculations of Sherman function for the e^{\pm} -CF₃I scattering are presented in the literature through our investigation. Energy dependence of absolute DCS and Sherman function are illustrated along with the available data. Failure of our energy dependent DCS calculations is observed below 10 eV due to the aforementioned reasons. A remarkable feature of our screening corrected calculation is that it shows excellent reproduction of electron impact total and transport cross-sections. In the case of positron impact TCS, our calculations underestimate the only available experimental observation below 10 eV. More data, both experimental and theoretical, are needed to bring out the more acceptable illustration of positron impact TCS. A comparison of the observable quantities is made to illustrate the similarities and differences between electron and positron collision with molecules. Most of the differences are observed to occur within a few hundred eV. The low energy electron impact scattering cross-sections possess greater value than those of positron impact. The cumulative effect of correlation-polarization and static potentials and the low energy contribution of exchange potential play a significant role in this issue. Broad shape resonance has noticeable contribution to the magnitude of electron impact TCS. Our calculations reproduce the broad shape resonance with a peak at around 6 eV in electron impact TCS but cannot reproduce the fine structures, arising due to Ps formation, excitation, and ionization, observed in positron impact TCS.

Sophisticated models using realistic projectile–molecule interactions perform better than our model at low energies at the expense of time consuming, strenuous computations. Although the code [21] used is not designed to calculate the cross sections for inelastic processes, such as excitation, ionization to specific electronic states, and dissociation, the advantage of our model is that it is an easy-to-implement recipe and can generate a broad spectrum of observable quantities with reasonable accuracy over a wide energy range. The success of IAM with the inclusion of screening correction in describing the projectile–molecule collision is encouraging. This easy-to-use recipe might be useful to mitigate the demand of the observable quantities related to the scattering of electrons and positrons off the diatomic and polyatomic molecules in many research and technical fields. More data are needed for further refinement of the theory.

Author Contributions: M.H.K.: investigation, formal analysis, and writing—original draft preparation and editing; M.M.K.: data curation and editing; M.M.B.: review and editing; M.M.H.: visualization; A.K.F.H.: methodology and supervision; H.W.: review and resources; M.A.U.: conceptualization, software, review, and validation. All authors have read and agreed to the submitted version of the manuscript.

Funding: This research received no external funding.

Conflicts of Interest: The authors declare no conflict of interest.

References

1. Christophorou, L.G.; Olthoff, J.K. *Fundamental Electron Interactions with Plasma Processing Gases*; Springer Science & Business Media: New York, NY, USA, 2012.
2. Lane, N. The theory of electron-molecule collisions. *Rev. Mod. Phys.* **1980**, *52*, 29. [[CrossRef](#)]

3. Miles, W.; Thompson, R.; Green, A. Electron-impact cross sections and energy deposition in molecular hydrogen. *J. Appl. Phys.* **1972**, *43*, 678–686. [[CrossRef](#)]
4. Dalgarno, A.; Yan, M.; Liu, W. Electron energy deposition in a gas mixture of atomic and molecular hydrogen and helium. *Astrophys. J. Suppl. Ser.* **1999**, *125*, 237. [[CrossRef](#)]
5. Khandker, M.H.; Arony, N.T.; Haque, A.; Maaza, M.; Billah, M.M.; Uddin, M.A. Scattering of e^{\pm} from N₂ in the energy range 1 eV–10 keV. *Mol. Phys.* **2020**, *118*, e1699183. [[CrossRef](#)]
6. Singh, S.; Dutta, S.; Naghma, R.; Antony, B. Positron scattering from simple molecules. *J. Phys. At. Mol. Phys.* **2017**, *50*, 135202. [[CrossRef](#)]
7. Antony, B.; Joshipura, K.; Mason, N. Total and ionization cross sections of electron scattering by fluorocarbons. *J. Phys. At. Mol. Opt. Phys.* **2005**, *38*, 189. [[CrossRef](#)]
8. Christophorou, L.G.; Olthoff, J.K. Electron interactions with CF₃I. *J. Phys. Chem. Ref. Data* **2000**, *29*, 553–569. [[CrossRef](#)]
9. Khare, S.P. *Introduction to the Theory of Collisions of Electrons with Atoms and Molecules*; Springer Science & Business Media: New York, NY, USA, 2002.
10. Jiang, Y.; Sun, J.; Wan, L. Additivity rule for the calculation of electron scattering from polyatomic molecules. *Phys. Rev. A* **2000**, *62*, 062712. [[CrossRef](#)]
11. Blanco, F.; Garcia, G. Screening corrections for calculation of electron scattering from polyatomic molecules. *Phys. Lett. A* **2003**, *317*, 458–462. [[CrossRef](#)]
12. Blanco, F.; Ellis-Gibbins, L.; García, G. Screening corrections for the interference contributions to the electron and positron scattering cross sections from polyatomic molecules. *Chem. Phys. Lett.* **2016**, *645*, 71–75. [[CrossRef](#)]
13. Billah, M.M.; Khandker, M.H.; Shorifuddoza, M.; Sayed, M.; Watabe, H.; Haque, A.; Uddin, M.A. Theoretical investigations of e^{\pm} -CO scattering. *J. Phys. B At. Mol. Opt. Phys.* **2021**, *54*, 095203. [[CrossRef](#)]
14. Billah, M.M.; Khatun, M.M.; Haque, M.; Ali, M.Y.; Khandker, M.H.; Haque, A.; Watabe, H.; Uddin, M.A. A Theoretical Study of Scattering of Electrons and Positrons by CO₂ Molecule. *Atoms* **2022**, *10*, 31. [[CrossRef](#)]
15. Akter, N.; Nure Alam Abdullah, M.; Shorifuddoza, M.; Patoary, M.A.R.; Masum Billah, M.; Khandker, M.H.; Maaza, M.; Watabe, H.; Haque, A.; Alfaz Uddin, M. Theoretical study of e^{\pm} -NH₃ scattering. *Mol. Phys.* **2022**, e2097135. [[CrossRef](#)]
16. Khandker, M.H.; Billah, M.M.; Watabe, H.; Haque, A.; Uddin, M.A. Theoretical studies on the elastic scattering of e^{\pm} off the ions of xenon isonuclear series. *Phys. Scr.* **2020**, *96*, 025402. [[CrossRef](#)]
17. Furness, J.; McCarthy, I. Semiphenomenological optical model for electron scattering on atoms. *J. Phys. At. Mol. Phys.* **1973**, *6*, 2280. [[CrossRef](#)]
18. Sun, J.; Yu, G.; Jiang, Y.; Zhang, S. Total cross-sections for positron scattering by a series of molecules. *Eur. Phys. J. D-At. Mol. Opt. Plasma Phys.* **1998**, *4*, 83–88. [[CrossRef](#)]
19. Perdew, J.P.; Zunger, A. Self-interaction correction to density-functional approximations for many-electron systems. *Phys. Rev. B* **1981**, *23*, 5048. [[CrossRef](#)]
20. Jain, A. Low-energy positron-argon collisions by using parameter-free positron correlation polarization potentials. *Phys. Rev. A* **1990**, *41*, 2437. [[CrossRef](#)]
21. Salvat, F.; Jablonski, A.; Powell, C.J. ELSEPA—Dirac partial-wave calculation of elastic scattering of electrons and positrons by atoms, positive ions and molecules. *Comput. Phys. Commun.* **2005**, *165*, 157–190. [[CrossRef](#)]
22. Underwood-Lemons, T.; Winkler, D.C.; Tossell, J.A.; Moore, J.H. Low-energy electron scattering cross sections of halofluorocarbons. *J. Chem. Phys.* **1994**, *100*, 9117–9122. [[CrossRef](#)]
23. Rozum, I.; Limao-Vieira, P.; Eden, S.; Tennyson, J.; Mason, N. Electron Interaction Cross Sections for CF₃I, C₂F₄, and CF_x (x = 1–3) Radicals. *J. Phys. Chem. Ref. Data* **2006**, *35*, 267–284. [[CrossRef](#)]
24. Kitajima, M.; Okamoto, M.; Sunohara, K.; Tanaka, H.; Cho, H.; Samukawa, S.; Eden, S.; Mason, N. Low-energy electron impact elastic and inelastic scattering from CF₃I. *J. Phys. B At. Mol. Opt. Phys.* **2002**, *35*, 3257. [[CrossRef](#)]
25. Francis-Staite, J.R.; Schmerl, B.A.; Brunger, M.J.; Kato, H.; Buckman, S.J. Elastic electron scattering from CF₃I. *Phys. Rev. A* **2010**, *81*, 022704. [[CrossRef](#)]
26. Cho, H.; Song, M.; Yoon, J.; Hoshino, M.; Tanaka, H. Elastic electron scattering from CF₃H and CF₃I. *J. Phys. B At. Mol. Opt. Phys.* **2010**, *43*, 135205. [[CrossRef](#)]
27. Kiataki, M.; do N. Varella, M.; Bettega, M.; Kossoski, F. Shape Resonances and Elastic Cross Sections in Electron Scattering by CF₃Br and CF₃I. *J. Phys. Chem. A* **2020**, *124*, 8660–8667. [[CrossRef](#)]
28. Nishimura, H.; Nakamura, Y. Total electron scattering cross sections for fluorofrom and trifluoroiodomethane. *J. Phys. Soc. Jpn.* **2005**, *74*, 1160–1169. [[CrossRef](#)]
29. Kawada, M.K.; Sueoka, O.; Kimura, M. Electron and positron scattering from CF₃I molecules below 600 eV: A comparison with CF₃H. *Chem. Phys. Lett.* **2000**, *330*, 34–40. [[CrossRef](#)]
30. Bettega, M.H.F.; Natalense, A.P.P.; Lima, M.A.P.; Ferreira, L.G. Elastic scattering of low-energy electrons by CF₃Cl, CF₃Br and CF₃I. *J. Phys. At. Mol. Opt. Phys.* **2003**, *36*, 1263. [[CrossRef](#)]
31. Salvat, F. Optical-model potential for electron and positron elastic scattering by atoms. *Phys. Rev. A* **2003**, *68*, 012708. [[CrossRef](#)]
32. Khandker, M.H.; Haque, A.F.; Haque, M.; Billah, M.M.; Watabe, H.; Uddin, M.A. Relativistic Study on the Scattering of e^{\pm} from Atoms and Ions of the Rn Isonuclear Series. *Atoms* **2021**, *9*, 59. [[CrossRef](#)]

33. Hahn, B.; Ravenhall, D.; Hofstadter, R. High-energy electron scattering and the charge distributions of selected nuclei. *Phys. Rev.* **1956**, *101*, 1131. [[CrossRef](#)]
34. Desclaux, J. A multiconfiguration relativistic Dirac-Fock program. *Comput. Phys. Commun.* **1975**, *9*, 31–45. [[CrossRef](#)]
35. Rose, M.E. *Relativistic Electron Theory*; John Wiley and Sons, Inc.: New York, NY, USA, 1961.
36. Salvat, F.; Fernández-Varea, J.; Williamson, W., Jr. Accurate numerical solution of the radial Schrödinger and Dirac wave equations. *Comput. Phys. Commun.* **1995**, *90*, 151–168. [[CrossRef](#)]
37. Walker, D. Relativistic effects in low energy electron scattering from atoms. *Adv. Phys.* **1971**, *20*, 257–323. [[CrossRef](#)]
38. Mott, N.F.; Massey, H.S.W. *The Theory of Atomic Collisions*; Clarendon Press: Oxford, UK, 1965; Volume 35.
39. Joshipura, K.; Vinodkumar, M.; Limbachiya, C.; Antony, B. Calculated total cross sections of electron-impact ionization and excitations in tetrahedral (XY_4) and SF_6 molecules. *Phys. Rev. A* **2004**, *69*, 022705. [[CrossRef](#)]
40. National Institute of Standards and Technology; Security Requirements for Cryptographic Modules. *Technical Report Federal Information Processing Standards Publications (FIPS PUBS) 140-2*; U.S. Department of Commerce: Washington, DC, USA, 2022.
41. Dapor, M.; Miotello, A. Differential, total, and transport cross sections for elastic scattering of low energy positrons by neutral atoms ($Z = 1-92$, $E = 500-4000$ eV). *At. Data Nucl. Data Tables* **1998**, *69*, 1–100. [[CrossRef](#)]
42. McEachran, R.; Stauffer, A.; Piwinski, M.; Pravica, L.; Williams, J.; Cvejanovic, D.; Samarin, S. Investigation of the behaviour of the Sherman function for elastic electron scattering from Kr and Xe. *J. Phys. At. Mol. Opt. Phys.* **2010**, *43*, 215208. [[CrossRef](#)]
43. Gorfinkiel, J.D.; Ptasinska, S. Electron scattering from molecules and molecular aggregates of biological relevance. *J. Phys. At. Mol. Opt. Phys.* **2017**, *50*, 182001. [[CrossRef](#)]
44. Mayol, R.; Salvat, F. Total and transport cross sections for elastic scattering of electrons by atoms. *At. Data Nucl. Data Tables* **1997**, *65*, 55–154. [[CrossRef](#)]
45. Jiao, C.; Ganguly, B.; DeJoseph, C., Jr.; Garscadden, A. Comparisons of electron impact ionization and ion chemistries of CF_3Br and CF_3I . *Int. J. Mass Spectrom.* **2001**, *208*, 127–133. [[CrossRef](#)]
46. Makochekanwa, C.; Sueoka, O.; Kimura, M. Similarities and differences between electron and positron scattering from molecules. *J. Physics Conf. Ser.* **2007**, *80*, 012012. [[CrossRef](#)]